AIM2 in regulatory T cells restrains autoimmune diseases

https://doi.org/10.1038/s41586-021-03231-w

Received: 20 June 2019

Accepted: 14 December 2020

Published online: 27 January 2021

Wei-Chun Chou[1,2,9], Zengli Guo[1,3,9], Hao Guo[1,2], Liang Chen[1,3], Ge Zhang[1,3], Kaixin Liang[1,4], Ling Xie[5], Xianming Tan[1], Sara A. Gibson[1], Elena Rampanelli[1,2], Yan Wang[1], Stephanie A. Montgomery[1,6], W. June Brickey[1,3], Meng Deng[1,4], Leslie Freeman[1,2], Song Zhang[1,3], Maureen A. Su[1,7,8], Xian Chen[5], Yisong Y. Wan[1,3]✉ & Jenny P.-Y. Ting[1,2,3,4]✉

The inflammasome initiates innate defence and inflammatory responses by activating caspase-1 and pyroptotic cell death in myeloid cells[1,2]. It consists of an innate immune receptor/sensor, pro-caspase-1, and a common adaptor molecule, ASC. Consistent with their pro-inflammatory function, caspase-1, ASC and the inflammasome component NLRP3 exacerbate autoimmunity during experimental autoimmune encephalomyelitis by enhancing the secretion of IL-1β and IL-18 in myeloid cells[3–6]. Here we show that the DNA-binding inflammasome receptor AIM2[7–10] has a T cell-intrinsic and inflammasome-independent role in the function of T regulatory (T_{reg}) cells. *AIM2* is highly expressed by both human and mouse T_{reg} cells, is induced by TGFβ, and its promoter is occupied by transcription factors that are associated with T_{reg} cells such as RUNX1, ETS1, BCL11B and CREB. RNA sequencing, biochemical and metabolic analyses demonstrated that AIM2 attenuates AKT phosphorylation, mTOR and MYC signalling, and glycolysis, but promotes oxidative phosphorylation of lipids in T_{reg} cells. Mechanistically, AIM2 interacts with the RACK1–PP2A phosphatase complex to restrain AKT phosphorylation. Lineage-tracing analysis demonstrates that AIM2 promotes the stability of T_{reg} cells during inflammation. Although AIM2 is generally accepted as an inflammasome effector in myeloid cells, our results demonstrate a T cell-intrinsic role of AIM2 in restraining autoimmunity by reducing AKT–mTOR signalling and altering immune metabolism to enhance the stability of T_{reg} cells.

Experimental autoimmune encephalomyelitis (EAE) was induced in wild-type, *Aim2*$^{-/-}$, *Asc*$^{-/-}$ (also known as *Pycard*$^{-/-}$), and double-knockout *Casp1*$^{-/-}$*Casp11*$^{-/-}$ (*Casp11* is also known as *Casp4*) mice after immunization with the myelin oligodendrocyte glycoprotein $(MOG)_{35-55}$ peptide (Methods). Consistent with the literature, *Asc*$^{-/-}$ and *Casp1*$^{-/-}$*Casp11*$^{-/-}$ mice had negligible EAE compared to wild-type controls[4,5] (Fig. 1a). Notably, *Aim2*$^{-/-}$ mice developed more severe EAE, with higher clinical score and disease incidence (Fig. 1a) and increased pathology, demyelination and inflammatory immune cell infiltration in the spinal cord when compared to wild-type control mice (Fig. 1b–d), whereas *Asc*$^{-/-}$ mice showed a reduction in all of these parameters (Fig. 1b, c). These observations questioned the predicted, pro-inflammatory role of AIM2 through inflammasome activation in EAE. Indeed, levels of the cytokines IL-1β, IL-18, IL-6 and TNF were indistinguishable in the spinal cords of *Aim2*$^{-/-}$ and control mice (Fig. 1e). T helper 1 (T_H1) and T_H17 cells promote whereas T_{reg} cells restrict the development of EAE[11]. Analysis of the CD4$^+$ T cell population in the spinal cords of diseased wild-type and *Aim2*$^{-/-}$ mice revealed that *Aim2*$^{-/-}$ mice had decreased numbers of FOXP3$^+$ T_{reg} cells and increased levels of IL-17A$^+$ and IL-17A$^+$IFNγ$^+$ CD4$^+$ T cells during the early phase of EAE (Fig. 1f, g). T_{reg}, T_H1 and T_H17 cells were not significantly different in the spleens and draining lymph nodes of wild-type and *Aim2*$^{-/-}$ mice (Extended Data Fig. 1a, b). Under steady-state conditions, *Aim2*$^{-/-}$ mice showed normal T cell homeostasis in the thymus, spleen and lymph nodes (Extended Data Fig. 1c–h). These findings indicate that AIM2-dependent changes in T cells occurred at sites of neuroinflammation. Although FOXP3$^+$ T_{reg} cells were reduced in the spinal cords of *Aim2*$^{-/-}$ mice during EAE (Fig. 1f), wild-type and *Aim2*$^{-/-}$ T_{reg} cells proliferated, survived and expressed effector markers similarly, under steady state and during EAE (Extended Data Fig. 2a–e). During the late phase of EAE, *Aim2* deletion led to reduced expression of *Foxp3*, *Tgfb1* and *Il10* mRNA (Fig. 1h) and IL-10 protein (Fig. 1i) in spinal cords. Consistently, the numbers of FOXP3$^+$ T_{reg} cells were significantly decreased in the spinal cords of *Aim2*$^{-/-}$ mice, whereas T_H17 cells were increased (Fig. 1j). *Aim2*$^{-/-}$ CD4$^+$ T cells proliferated normally in vitro (Extended Data Fig. 2f, g) and *Aim2*$^{-/-}$ CD8$^+$ T cells were phenotypically normal during EAE (Extended Data Fig. 2h–k). We therefore posit that AIM2 probably controls CD4$^+$ T cell function to mitigate EAE.

[1]Lineberger Comprehensive Cancer Center, University of North Carolina at Chapel Hill, Chapel Hill, NC, USA. [2]Department of Genetics, University of North Carolina at Chapel Hill, Chapel Hill, NC, USA. [3]Department of Microbiology and Immunology, University of North Carolina at Chapel Hill, Chapel Hill, NC, USA. [4]Oral and Craniofacial Biomedicine Program, School of Dentistry, University of North Carolina at Chapel Hill, Chapel Hill, NC, USA. [5]Department of Biochemistry and Biophysics, University of North Carolina at Chapel Hill, Chapel Hill, NC, USA. [6]Department of Pathology and Laboratory Medicine, University of North Carolina at Chapel Hill, Chapel Hill, NC, USA. [7]Department of Pediatrics, University of North Carolina at Chapel Hill, Chapel Hill, NC, USA. [8]Present address: Department of Microbiology Immunology and Medical Genetics and Pediatrics, David Geffen School of Medicine at UCLA, Los Angeles, CA, USA. [9]These authors contributed equally: Wei-Chun Chou, Zengli Guo. ✉e-mail: wany@email.unc.edu; jenny_ting@med.unc.edu

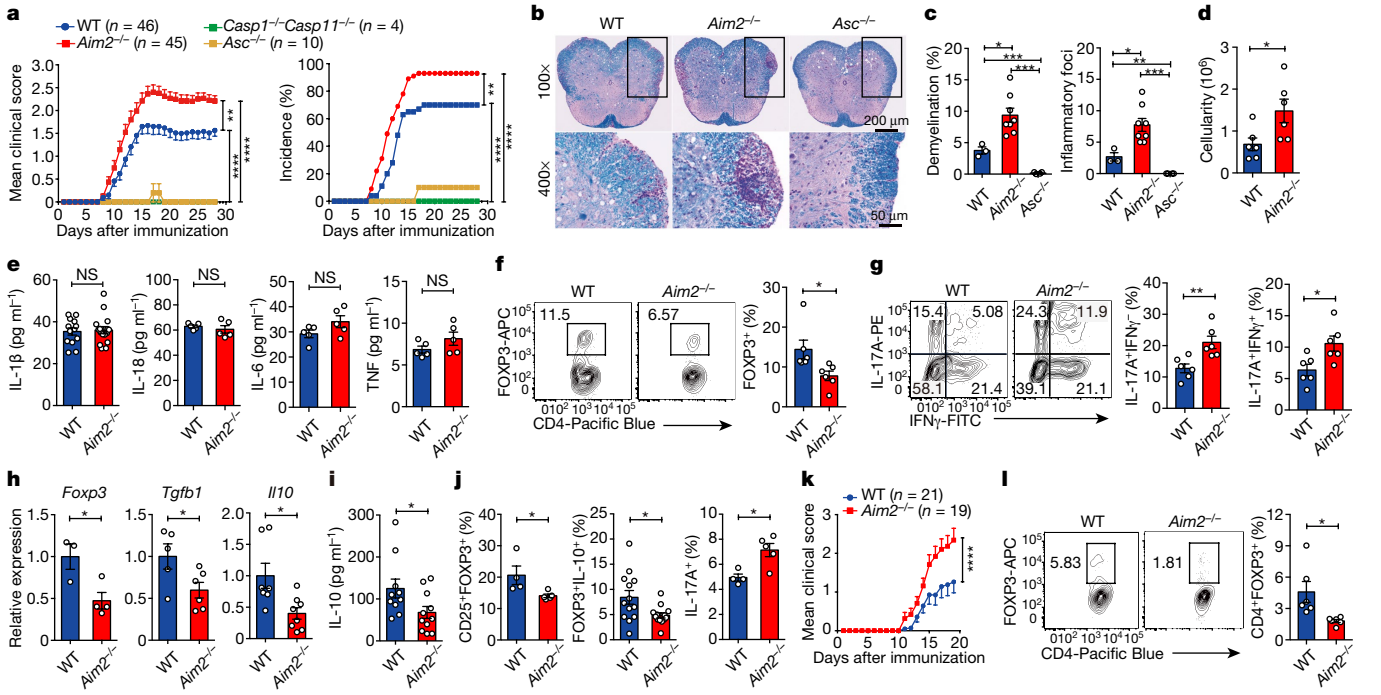

Fig. 1 | *Aim2*$^{-/-}$ and *Asc*$^{-/-}$ mice have opposing responses to EAE. a, EAE scoring of wild-type (WT) ($n = 46$), *Aim2*$^{-/-}$ ($n = 45$), *Asc*$^{-/-}$ ($n = 10$) and *Casp1*$^{-/-}$*Casp11*$^{-/-}$ ($n = 4$) mice; five experiments for WT and *Aim2*$^{-/-}$ mice, two experiments for *Asc*$^{-/-}$ mice and one experiment for *Casp1*$^{-/-}$*Casp11*$^{-/-}$ mice. The last two strains produced results that are consistent with previous reports[4,5]. **b**, Luxol fast blue and periodic acid-Schiff (LFB-PAS) staining of spinal cords. WT ($n = 3$), *Aim2*$^{-/-}$ ($n = 8$) and *Asc*$^{-/-}$ ($n = 4$) mice, day 22 of EAE. Representative of 3–8 mice per group, three experiments. **c**, Quantification of demyelination and inflammatory foci. WT ($n = 3$), *Aim2*$^{-/-}$ ($n = 8$) and *Asc*$^{-/-}$ ($n = 4$) mice from **b**. **d**, Infiltrating cells in spinal cords of wild-type and *Aim2*$^{-/-}$ mice, day 22 of EAE, $n = 6$ per group, two experiments. **e**, Spinal cord IL-1β, IL-18, IL-6 and TNF, analysed by ELISA; WT ($n = 13$) and *Aim2*$^{-/-}$ ($n = 16$) for IL-1β (3 experiments), $n = 5$ for other cytokines (2 experiments). **f**, **g**, Flow cytometry of CD4$^+$FOXP3$^+$ T$_{reg}$ cells (**f**), IFNγ$^+$ or IL-17A$^+$ CD4$^+$ cells (**g**) in spinal cords of wild-type and *Aim2*$^{-/-}$ mice, days 14–15 during EAE, $n = 6$ per group, three experiments. **h**, qRT–PCR of indicated genes, $n = 3$, 5 and 6 for WT, $n = 4$, 6 and 8 for *Aim2*$^{-/-}$ samples, two experiments. **i**, IL-10 protein analysed by ELISA; $n = 10$ for WT and 11 for *Aim2*$^{-/-}$ samples, three experiments. **j**, Flow cytometry of CD25$^+$FOXP3$^+$, FOXP3$^+$IL-10$^+$ and IL-17A$^+$CD4$^+$ cells in wild-type and *Aim2*$^{-/-}$ spinal cords at days 22–23 of EAE, $n = 4$ for WT, $n = 5$ for *Aim2*$^{-/-}$ samples of CD25$^+$FOXP3$^+$ and IL-17A$^+$ (2 experiments), $n = 13$ per group for FOXP3$^+$IL-10$^+$ (3 experiments). **k**, EAE scores of *Rag1*$^{-/-}$ mice that received wild-type ($n = 21$) or *Aim2*$^{-/-}$ CD4$^+$ T cells ($n = 19$), three experiments. **l**, Flow cytometry of spinal cord CD4$^+$FOXP3$^+$ T$_{reg}$ cells from **k**, $n = 6$ per group, three experiments. Data are mean ± s.e.m. NS, not significant. *$P < 0.05$, **$P < 0.01$, ***$P < 0.001$, ****$P < 0.0001$, two-way ANOVA and Holm–Sidak post hoc test (**a**, **k**), two-sided *t* test (**c**–**j**, **l**).

To assess the CD4$^+$ T cell-intrinsic function of AIM2, we adoptively transferred CD4$^+$ T cells from wild-type or *Aim2*$^{-/-}$ mice into *Rag1*$^{-/-}$ mice[12] followed by EAE elicitation. Mice that received *Aim2*$^{-/-}$ CD4$^+$ T cells developed more severe EAE at an earlier time than those that received wild-type CD4$^+$ T cells (Fig. 1k), with concurrent reduced T$_{reg}$ cells in the spinal cord (Fig. 1l). These findings suggest a previously unappreciated cell-intrinsic function of AIM2 in T$_{reg}$ cells. High levels of *Aim2* expression are detected in both mouse (https://www.immgen.org/)[13] and human (https://www.ebi.ac.uk)[14] T$_{reg}$ cells (Extended Data Fig. 3a–c). We empirically confirmed that isolated T$_{reg}$ cells expressed higher levels of *Aim2* than CD4$^+$ conventional T (T$_{conv}$) cells, with or without T cell receptor (TCR) activation (Extended Data Fig. 3d–f). Notably, TGFβ, a factor that is vital for T$_{reg}$ cell generation and homeostasis[15], increased *Aim2* expression in CD4$^+$, but not in CD8$^+$ T cells. Furthermore, genetic abrogation of TGFβ signalling in mice with deletion of the *Tgfbr2* gene reduced *Aim2* expression in T$_{reg}$ cells in vivo (Extended Data Fig. 3g–i). Analysis of chromatin immunoprecipitation followed by high-throughput sequencing (ChIP–seq) datasets (DRP003376)[16] of the *Aim2* promoter in T$_{reg}$ versus T$_{conv}$ cells showed that the transcription factors RUNX1, EST1, BCL11B and CREB, which are known to bind the *Foxp3* loci to regulate T$_{reg}$ cell stability[16–18], also bound to the *Aim2* promoter in T$_{reg}$ cells more than in T$_{conv}$ cells (Extended Data Fig. 3j). These findings suggest that a T$_{reg}$ cell-specific molecular network favours *Aim2* expression.

To assess the function of AIM2 in T$_{reg}$ cells, we first studied a T cell-induced colitis model in which transferred naive T cells provoke colitis in *Rag1*$^{-/-}$ recipients, whereas the inclusion of T$_{reg}$ cells offers protection[19]. CD4$^+$CD45RB^{hi} naive T cells from wild-type mice were transferred alone or with sorted wild-type or *Aim2*$^{-/-}$ T$_{reg}$ cells into *Rag1*$^{-/-}$ recipients (Fig. 2a). Transferred wild-type naive T cells led to a decline in the body weight of recipient mice (Fig. 2b) and intestinal pathology (Extended Data Fig. 4a, b). Transferred *Aim2*$^{-/-}$ T$_{reg}$ cells in the colon were present at a reduced frequency compared to wild-type T$_{reg}$ cells (Fig. 2c). The inclusion of wild-type but not *Aim2*$^{-/-}$ T$_{reg}$ cells mitigated weight loss (Fig. 2b), reduced pathology and suppressed the expression of pro-inflammatory cytokines IL-1α, IL-1β, TNF, IL-12 and IFNγ, but promoted anti-inflammatory IL-10 in colon explants (Extended Data Fig. 4a–c). To determine whether the role of AIM2 in T$_{reg}$ cells can be separated from its conventional role in inflammasome activation, we transferred *Asc*$^{-/-}$ T$_{reg}$ cells in the colitis model. In contrast to *Aim2*$^{-/-}$ T$_{reg}$ cells, *Asc*$^{-/-}$ T$_{reg}$ cells had similar effects to wild-type T$_{reg}$ cells (Extended Data Fig. 4d, e).

We next examined the function of AIM2 in T$_{reg}$ cells in the EAE model. Naive CD4$^+$ T cells from 2D2 mice that expressed a transgenic T cell receptor for the encephalitogenic autoantigen, MOG$_{35–55}$, were transferred with sorted T$_{reg}$ cells from either wild-type or *Aim2*$^{-/-}$ mice into *Rag1*$^{-/-}$ recipients. EAE was then elicited in these recipient mice (Extended Data Fig. 4f, g). Mice that received 2D2 CD4$^+$ T cells alone developed severe EAE (Extended Data Fig. 4h). The addition of wild-type T$_{reg}$ cells modestly attenuated EAE development (Extended Data Fig. 4h), with a decrease in T$_H$17 cells and an increase in T$_{reg}$ cells in the spinal cord (Extended Data Fig. 4i, j). By contrast, *Aim2*$^{-/-}$ T$_{reg}$ cells were unable to reduce EAE (Extended Data Fig. 4g–j). Notably,

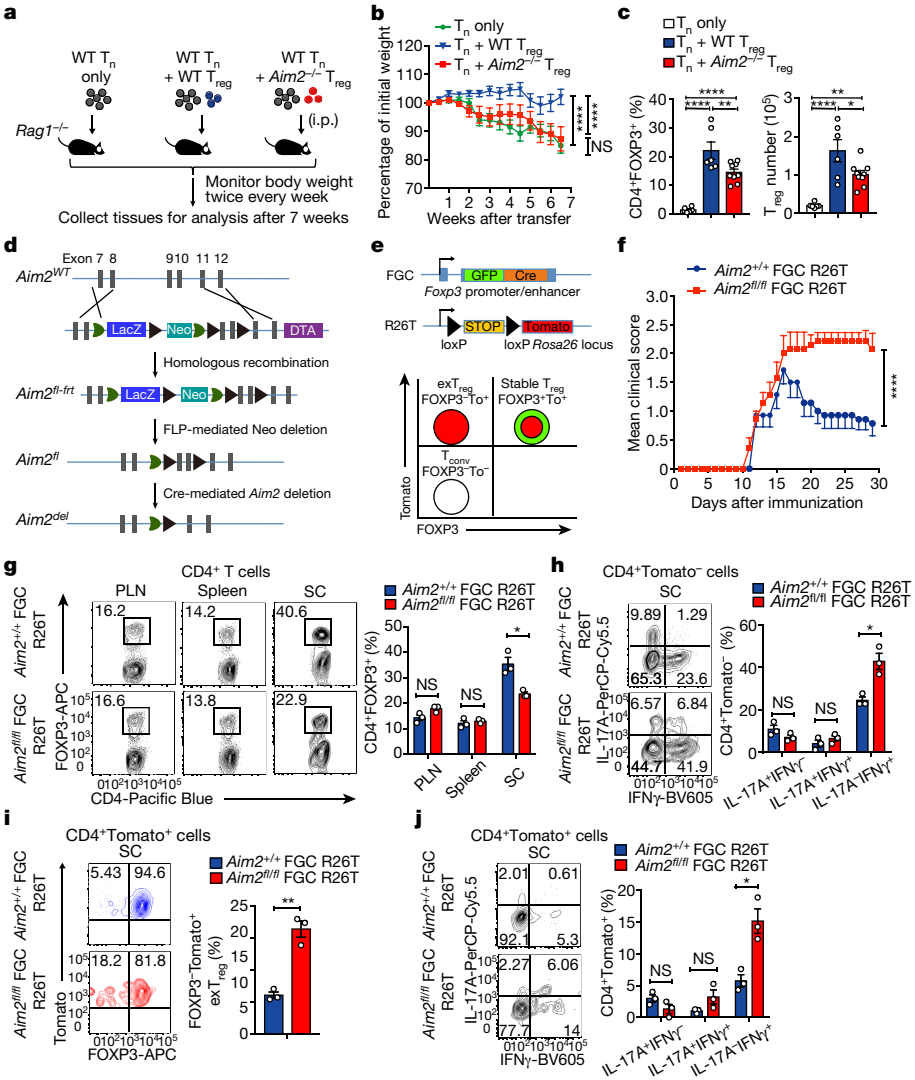

Fig. 2 | AIM2 stabilizes T_{reg} cells to restrain autoimmunity. a, Schematic of wild-type $CD4^+CD45RB^{hi}$ naive T (T_n) cell-induced colitis, with or without T_{reg} cells. **b**, Body weight of *Rag1*$^{-/-}$ mice that received T_n cells ($n = 8$), T_n + WT T_{reg} cells ($n = 8$), or T_n + *Aim2*$^{-/-}$ T_{reg} cells ($n = 9$); two experiments. **c**, Flow cytometry of $CD4^+FOXP3^+$ T_{reg} cells in colons of *Rag1*$^{-/-}$ mice that received T_n ($n = 6$), T_n + WT T_{reg} cells ($n = 6$), T_n + *Aim2*$^{-/-}$ T_{reg} cells ($n = 9$), 7 weeks after transfer, two experiments. **d**, Schema for gene targeting to generate floxed *Aim2* mice. **e**, Top, schema for generating FOXP3 T_{reg} lineage-tracing mice. Bottom, T_{conv} cells, stable T_{reg} cells and exT_{reg} cells based on FOXP3 and Tomato (To) expression. **f**, EAE scores of mice of indicated genotypes ($n = 7$ per group); two experiments. **g**, Flow cytometry of FOXP3 expression in $CD4^+$ cells in peripheral lymph node (PLN), spleen, and spinal cord (SC) of mice of indicated genotypes at day 28 of EAE, $n = 3$ experiments. **h**, Flow cytometry of IFNγ and IL-17A production in $CD4^+Tomato^-$ T cells in spinal cords of mice of indicated genotypes at day 28 of EAE, $n = 3$ experiments. **i**, Flow cytometry of FOXP3 production in $CD4^+Tomato^+$ T cells in spinal cords of mice of indicated genotypes at day 28 of EAE, $n = 3$ experiments. **j**, Flow cytometry of IFNγ and IL-17A production in $CD4^+Tomato^+$ T cells in spinal cords of mice of indicated genotypes at day 28 of EAE, $n = 3$ experiments. Data are mean ± s.e.m. $^*P < 0.05$, $^{**}P < 0.01$, $^{****}P < 0.0001$, two-way ANOVA and Holm–Sidak post hoc test (**b**, **f**), one-way ANOVA with Tukey's multiple comparisons test (**c**), multiple *t*-test corrected by the Holm–Sadik method (**g**, **h**, **j**), unpaired *t* test (**i**).

transferred *Aim2*$^{-/-}$ T_{reg} cells gained expression of IL-17A but had reduced populations of $IL\text{-}17A^-IFN\gamma^-$ cells (Extended Data Fig. 4k). These findings suggest a crucial role for AIM2 in promoting T_{reg} cell function in vivo. However, the in vitro suppressive function of *Aim2*$^{-/-}$ T_{reg} cells appeared normal (Extended Data Fig. 4l).

Wild-type T_{reg} cells did not strongly suppress EAE in 2D2 mice, probably owing to robust T cell activation mediated by the transgenic TCR expressed in these mice. To better address the T_{reg} cell-intrinsic role of AIM2, we generated mice with T_{reg} cell-specific deletion by creating a mouse strain with a floxed *Aim2* allele by gene targeting (Fig. 2d). Mice with a floxed *Aim2* allele were bred with mice bearing a T_{reg}-specific Cre transgene *Foxp3-GFP-cre* (FGC) and with mice bearing the *Rosa26*^{tdTomato} (R26T) lineage-tracing allele (Fig. 2e). T_{reg} cell-specific deletion of *Aim2* was confirmed by PCR and western blot (Extended Data Fig. 5a, b). T_{reg} cell-specific *Aim2*$^{-/-}$ mice were normal without any obvious defects under steady-state conditions (Extended Data Fig. 5c–i). EAE elicitation resulted in significantly higher clinical scores in T_{reg} cell-specific *Aim2*$^{-/-}$ mice compared to wild-type mice, accompanied by lower $FOXP3^+$ T_{reg} cells and higher $IFN\gamma^+CD4^+$ T cells in the spinal cord (Fig. 2g, h). *Aim2*$^{+/+}$ FGC R26T and *Aim2*$^{fl/fl}$ FGC R26T mice were used for lineage tracing based on the schematic depicted in Fig. 2e. *Aim2* deletion led to increased levels of exT_{reg} cells ($FOXP3^-Tomato^+$ cells that previously expressed FOXP3) and increased IFNγ expression by T_{reg} cells in the spinal cord (Fig. 2i, j), but not the spleen or draining lymph nodes during EAE (Extended Data Fig. 5j, k). *Aim2*-deficient T_{reg} cells proliferated and survived normally during EAE and under steady-state conditions (Extended Data Fig. 5l–o). These findings support a crucial biological role for AIM2 in promoting T_{reg} cell stability.

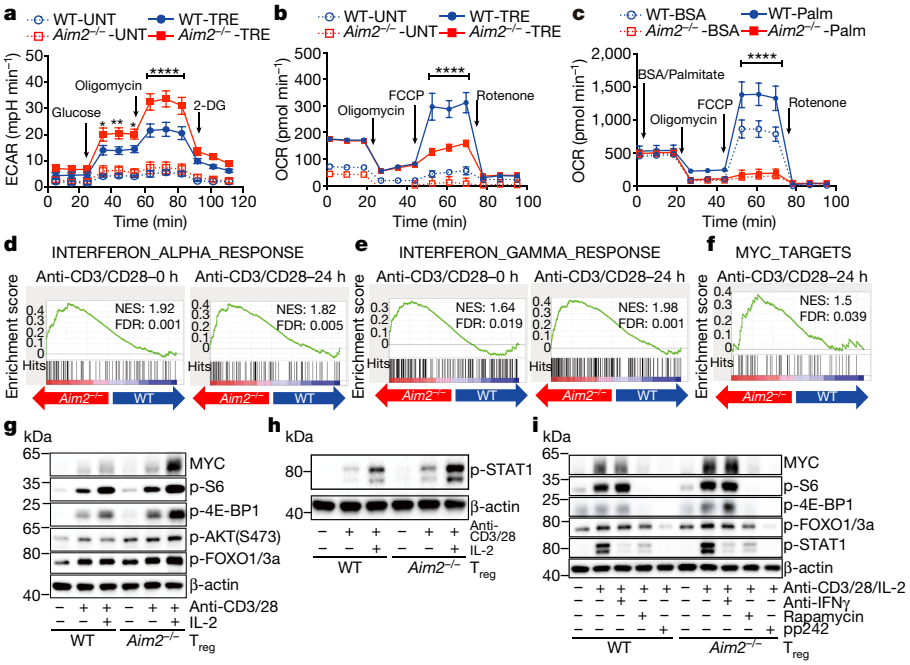

Fig. 3 | AIM2 regulates immune metabolism, AKT–mTOR and IFN signalling in T_{reg} cells isolated in vivo. a, Glycolytic activity of wild-type ($n = 7$ experiments) and *Aim2*$^{-/-}$ ($n = 6$ experiments) CD4$^+$CD25$^+$ T_{reg} cells untreated (UNT) or treated (TRE) with anti-CD3/CD28 plus IL-2 (500 U ml^{-1}) for 24 h. 2-DG, 2-deoxyglucose. **b**, OCR of wild-type ($n = 3$ experiments) and *Aim2*$^{-/-}$ ($n = 4$ experiments) CD4$^+$CD25$^+$ T_{reg} cells with or without anti-CD3/CD28 plus IL-2 (500 U ml^{-1}) for 24 h. **c**, Fatty acid oxidation of wild-type ($n = 5$ experiments) and *Aim2*$^{-/-}$ ($n = 6$ experiments) CD4$^+$CD25$^+$ T_{reg} cells with or without anti-CD3/CD28 plus IL-2 (500 U ml^{-1}) for 24 h. Cells were starved in substrate-limited medium and given only bovine serum albumin (BSA) or palmitate-BSA in fatty acid oxidation assay medium, and OCR was measured to indicate oxidation of fatty acids (Methods). **d**–**f**, Enrichment of IFNα response signatures (**d**), IFNγ response signatures (**e**), and MYC-related targets (**f**) by GSEA of RNA-seq datasets from *Aim2*$^{-/-}$ and wild-type T_{reg} cells stimulated with anti-CD3/CD28 antibodies plus IL-2 (500 U ml^{-1}). FDR, false discovery rate; NES, normalized enrichment score. **g**, Immunoblot analysis of indicated proteins in wild-type and *Aim2*$^{-/-}$ CD4$^+$CD25$^+$ T_{reg} cells with or without anti-CD3/CD28 plus IL-2 (500 U ml^{-1}) for 24 h. Data are representative of three experiments. **h**, Immunoblot analysis of p-STAT1 and β-actin in wild-type and *Aim2*$^{-/-}$ CD4$^+$CD25$^+$ T_{reg} cells treated as described in **g**. Data are representative of three experiments. **i**, Immunoblot analysis of indicated proteins in wild-type and *Aim2*$^{-/-}$ CD4$^+$CD25$^+$ T_{reg} cells stimulated with anti-CD3/CD28 plus IL-2 (500 U ml^{-1}) in the presence of rapamycin (1 nM), pp242 (0.5 μM) or anti-IFNγ antibody (XMG1.2, 10 μg ml^{-1}) for 24 h. Data are representative of three experiments. Data are mean ± s.e.m. *$P < 0.05$, **$P < 0.01$, ****$P < 0.0001$, two-way ANOVA (**a**–**c**).

We next explored the mechanisms by which AIM2 regulates T_{reg} cells. Previous studies found that AIM2 could attenuate AKT activation in gastrointestinal epithelial cells[20,21]. AKT–mTOR signalling positively associates with glycolytic metabolism, which negatively affects T_{reg} cell function[22]. To investigate whether *Aim2* deletion altered T_{reg} cell metabolism, wild-type or *Aim2*$^{-/-}$ T_{reg} cells were activated by TCR stimulation. *Aim2*$^{-/-}$ T_{reg} cells showed higher glycolytic activity assessed by the extracellular acidification rate (ECAR) (Fig. 3a, quantified in Extended Data Fig. 6a) compared to wild-type T_{reg} cells. *Aim2*$^{-/-}$ T_{reg} cells also had reduced oxygen consumption rate (OCR) and fatty acid oxidation (Fig. 3b, c), indicating impaired lipid oxidative phosphorylation and increased aerobic glycolysis[23]. Global transcriptional profiling by RNA sequencing (RNA-seq) and gene set enrichment analysis (GSEA) revealed that *Aim2* deletion led to enhanced interferon (IFN)-responsive signatures (Fig. 3d, e, Extended Data Fig. 6b, c), including IRF1 and IFNγ, both of which are known to attenuate *Foxp3* expression and T_{reg} cell function[24,25], as well as enhanced MYC-dependent programming[26] (Fig. 3f, Extended Data Fig. 6d). Consistently, *Aim2*$^{-/-}$ T_{reg} cells had increased expression of MYC protein[26], hyperphosphorylation of S6 and 4E-BP1 (an indicator of mTORC1 signalling), and increased levels of phosphorylated AKT (p-AKT) and its downstream targets p-FOXO1 and p-FOXO3A (Fig. 3g), which can block *Foxp3* expression[27]. In addition, p-STAT1, a factor indicative of IFN signalling, was increased in *Aim2*$^{-/-}$ T_{reg} cells (Fig. 3h). Enhanced mTOR, but not IFNγ, appeared to be central to—and causal for—the above-mentioned alterations in *Aim2*$^{-/-}$ T cells because treatment with pharmacological inhibitors of mTORC1 (rapamycin) or mTORC1/2 (pp242) blocked excessive MYC, p-S6, p-4E-BP1, p-FOXO1, p-FOXO3A and p-STAT1, whereas anti-IFNγ neutralization only blocked p-STAT1 (Fig. 3i).

We then examined whether AIM2 also controls de novo T_{reg} cell generation by treating wild-type or *Aim2*$^{-/-}$ CD4$^+$ T cells with TGFβ in vitro. Compared to wild-type cells, fewer *Aim2*$^{-/-}$ CD4$^+$ T cells differentiated into FOXP3$^+$ cells in the presence of TGFβ (Fig. 4a, b) whereas T_H1 and T_H17 cell differentiation were similar between wild-type and *Aim2*$^{-/-}$ cells (Fig. 4c, Extended Data Fig. 7a). To understand how AIM2 controls TGFβ-induced T_{reg} cell generation, we performed RNA-seq analysis to compare gene expression profiles of wild-type and *Aim2*$^{-/-}$ CD4$^+$ T cells activated by TGFβ. The analysis revealed that pathways involving PI3K–AKT–mTOR, mTORC1, glycolysis, MYC and IFNs are among the top pathways preferentially upregulated in TGFβ-induced *Aim2*$^{-/-}$ T_{reg} cells (Fig. 4d, Extended Data Figs. 7b–d, 8a–d).

Because TGFβ-induced T_{reg} cell differentiation is under metabolic control[28], we investigated whether AIM2 regulates metabolism during such a process. Indeed, TGFβ-induced *Aim2*$^{-/-}$ T_{reg} cells showed higher ECAR and glycolytic activity, but reduced OCR and fatty acid oxidation, when compared to wild-type cells (Fig. 4e–g), agreeing with what was observed in T_{reg} cells isolated from mice. In addition, AKT–mTOR signalling-related molecular markers, including MYC, p-S6, p-4E-BP1, p-AKT, p-FOXO1 and p-FOXO3A, were upregulated in the absence of AIM2 (Fig. 4h). Biochemical analyses of CD4$^+$ but not CD8$^+$ T cells revealed modestly enhanced AKT–mTOR signalling after AIM2 deletion 24 h after stimulation in vitro (Extended Data Fig. 9a, b).

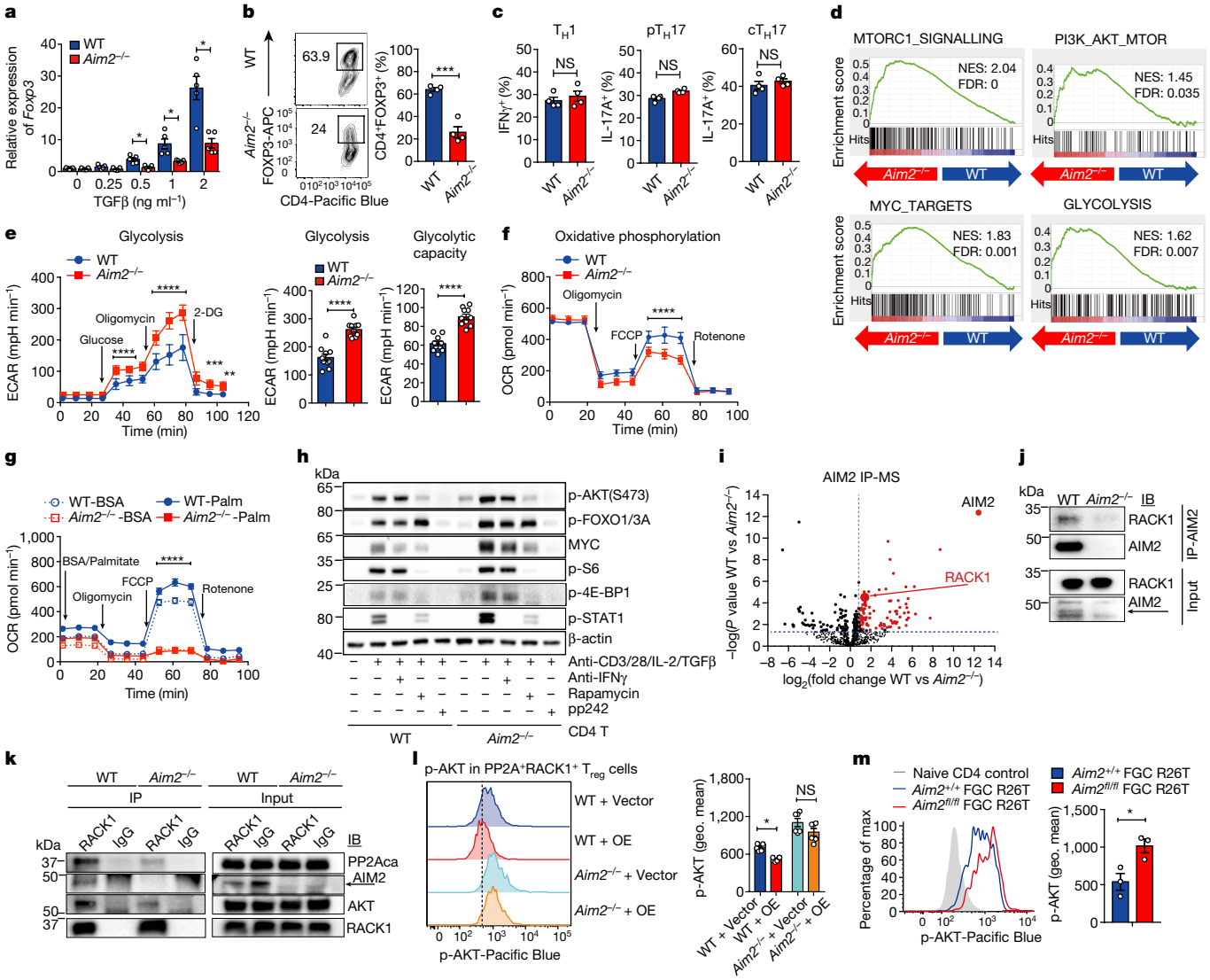

Fig. 4 | AIM2 promotes T_{reg} cells in vitro and restrains AKT–mTOR via the RACK1–PP2A complex. a, **b**, RT–PCR (**a**) and flow cytometry (**b**) of FOXP3 in wild-type and *Aim2*$^{-/-}$ CD4$^+$ T cells activated with the indicated amounts (**a**) or 2 ng ml^{-1} (**b**) of TGFβ for 4 days; $n = 5$ experiments in **a** and $n = 4$ experiments in **b**. **c**, Flow cytometry of IFNγ$^+$ or IL-17A$^+$ CD4$^+$ T cells of indicated genotypes, 4 days after differentiation under indicated polarizing conditions; $n = 4$ experiments. cT_H17, classic T_H17; pT_H17, pathogenic T_H17. **d**–**g**, Wild-type and *Aim2*$^{-/-}$ CD4$^+$ T cells were stimulated as in **b**. **d**, Enrichment scores of indicated gene sets, based on RNA-seq datasets. **e**, **f**, ECAR (**e**) and OCR (**f**) levels during glycolysis, and OCR levels during fatty acid oxidation (**g**), by Seahorse analysis; $n = 10$ experiments for **e**; $n = 5$ experiments for **f**; and $n = 3$ experiments for **g**. **h**, Immunoblotting of indicated proteins in wild-type and *Aim2*$^{-/-}$ CD4$^+$ T cells stimulated as in **b** with indicated treatment for 24 h. Representative of three experiments. **i**, Volcano plot of AIM2-interacting proteins by immunoprecipitation–mass spectrometry (IP–MS) analysis. Red indicates significantly enriched proteins (log_2-transformed fold change > 1; *t*-test adjusted $P < 0.05$). **j**, **k**, The interactions of indicated proteins determined by immunoprecipitation using anti-AIM2 (**j**) or anti-RACK1 (**k**), in wild-type and *Aim2*$^{-/-}$ CD4$^+$ T cells activated with TGFβ for 24 h. PP2Aca, catalytic subunit of PP2A. Representative of three experiments. **l**, Flow cytometry of p-AKT levels (geometric mean) in wild-type and *Aim2*$^{-/-}$ T_{reg} cells transduced with PP2A and RACK1-expressing vector (OE) or vector; $n = 6$ experiments. **m**, Flow cytometry of p-AKT in spinal cord T_{reg} cells from mice of indicated genotypes, 28 days after EAE induction, $n = 3$ experiments. Data are mean ± s.e.m. $^*P < 0.05$, $^{**}P < 0.01$, $^{***}P < 0.001$ $^{****}P < 0.0001$, two-sided *t*-test (**a**–**c**, **e** right, **m** right), two-way ANOVA (**e** left, **f**, **g**), multiple unpaired *t*-test with Holm–Sidak method (**l**).

In addition, *Aim2* deletion consistently led to increased AKT–mTOR signalling in T_{reg} cells (Extended Data Fig. 9c) but not in T_{conv} cells or CD8$^+$ cells (Extended Data Fig. 9d, e) at early time points, further highlighting a preferential role for AIM2 in controlling T_{reg} cell function. The pharmacological mTOR inhibitors, rapamycin and pp242, neutralized these changes in CD4$^+$ cells and reduced p-STAT1, whereas addition of the anti-IFNγ antibody (XMG1.2) only decreased p-STAT1 (Fig. 4h). These results indicate that IFNγ lies downstream of mTOR. Importantly, rapamycin or pp242 treatment restored TGFβ-induced T_{reg} cell differentiation to a normal level, suggesting that heightened mTOR activity due to *Aim2* deletion accounts for defective TGFβ-induced T_{reg} cell differentiation (Extended Data Fig. 10a). These findings suggest that AIM2 controls T_{reg} cell generation and function via the unified mechanism of AKT–mTOR restriction.

To investigate the molecular mechanism by which AIM2 regulates AKT–mTOR, we performed an unbiased mass spectrometric analysis to identify AIM2-interacting proteins during T_{reg} cell differentiation, using a mouse-specific anti-AIM2 antibody for endogenous immunoprecipitation from wild-type and *Aim2*$^{-/-}$ lysates under TGFβ-induced T_{reg} cell differentiation conditions (Extended Data Fig. 10b). One of the strongest AIM2-interacting proteins identified was RACK1 (Fig. 4i), which was validated by bi-directional endogenous co-immunoprecipitation (Fig. 4j, k). RACK1 promotes AKT dephosphorylation by recruiting the phosphatase PP2A[29], which dephosphorylates AKT and reduces mTOR

signalling to promote T_{reg} cells[30]. Reduced RACK1–PP2A interaction is therefore expected to increase AKT phosphorylation. Although the interaction of RACK1 with PP2A and AKT occurred normally in wild-type T_{reg} cells, this interaction was reduced in *Aim2*$^{-/-}$ T_{reg} cells (Fig. 4k). The specific interaction between AIM2 and the RACK1–PP2A–AKT complex was observed in TGFβ-induced T_{reg} conditions, but not in conventional T cells (Extended Data Fig. 10c). To test the function of RACK1 and PP2A, we ectopically expressed both proteins in TGFβ-induced T_{reg} cells and analysed the phosphorylation of AKT (p-AKT). Ectopic expression of RACK1 and PP2A downregulated p-AKT only in wild-type, and not in *Aim2*$^{-/-}$ T_{reg} cells, indicating that the effect of RACK1–PP2A on p-AKT was AIM2-dependent (Fig. 4l, Extended Data Fig. 10d, e). In agreement with the observed enhanced p-AKT in *Aim2*$^{-/-}$ T_{reg} cells in vitro, p-AKT was increased in *Aim2*$^{-/-}$ T_{reg} cells compared to wild-type controls in spinal cords during EAE (Fig. 4m). Therefore, hyperactivation of AKT in *Aim2*$^{-/-}$ T_{reg} cells in vitro and in vivo (Figs. 3g, 4h, m) can be attributed to an AIM2-dependent AKT dephosphorylation by the RACK1–PP2A complex[29].

In summary, AIM2 is an inflammasome effector in myeloid cells but its role in T cells has not been explored. This study reveals a previously unappreciated role of AIM2 in T_{reg} cells. It unveils a T_{reg} cell-intrinsic, inflammasome-independent function of AIM2 that promotes T_{reg} cells to control autoimmunity, specifically in models of multiple sclerosis and inflammatory bowel disease. We demonstrated the mechanism of AIM2 function in T_{reg} cells at three levels. At the cellular level, lineage-tracing analysis indicates that AIM2 is needed for the stability of T_{reg} cells. At the molecular and metabolic level, AIM2 attenuates the AKT–mTOR pathway to favour oxidative phosphorylation and fatty acid oxidation while mitigating glycolysis, thereby affecting immunometabolism profiles that favour T_{reg} cells. At the biochemical level, AIM2 promotes the association of AKT with the RACK1–PP2A axis to restrain AKT activation, thus reprogramming immunometabolism to favour T_{reg} cell function (model in Extended Data Fig. 10f).

Online content

Any methods, additional references, Nature Research reporting summaries, source data, extended data, supplementary information, acknowledgements, peer review information; details of author contributions and competing interests; and statements of data and code availability are available at https://doi.org/10.1038/s41586-021-03231-w.

1. Guo, H., Callaway, J. B. & Ting, J. P. Inflammasomes: mechanism of action, role in disease, and therapeutics. *Nat. Med.* **21**, 677–687 (2015).
2. Broz, P. & Dixit, V. M. Inflammasomes: mechanism of assembly, regulation and signalling. *Nat. Rev. Immunol.* **16**, 407–420 (2016).
3. Gris, D. et al. NLRP3 plays a critical role in the development of experimental autoimmune encephalomyelitis by mediating Th1 and Th17 responses. *J. Immunol.* **185**, 974–981 (2010).
4. Furlan, R. et al. Caspase-1 regulates the inflammatory process leading to autoimmune demyelination. *J. Immunol.* **163**, 2403–2409 (1999).
5. Shaw, P. J. et al. Cutting edge: critical role for PYCARD/ASC in the development of experimental autoimmune encephalomyelitis. *J. Immunol.* **184**, 4610–4614 (2010).
6. Martin, B. N. et al. T cell-intrinsic ASC critically promotes T_H17-mediated experimental autoimmune encephalomyelitis. *Nat. Immunol.* **17**, 583–592 (2016).
7. Fernandes-Alnemri, T., Yu, J. W., Datta, P., Wu, J. & Alnemri, E. S. AIM2 activates the inflammasome and cell death in response to cytoplasmic DNA. *Nature* **458**, 509–513 (2009).
8. Fernandes-Alnemri, T. et al. The AIM2 inflammasome is critical for innate immunity to *Francisella tularensis*. *Nat. Immunol.* **11**, 385–393 (2010).
9. Krieg, A. M. AIMing 2 defend against intracellular pathogens. *Nat. Immunol.* **11**, 367–369 (2010).
10. Rathinam, V. A. et al. The AIM2 inflammasome is essential for host defense against cytosolic bacteria and DNA viruses. *Nat. Immunol.* **11**, 395–402 (2010).
11. Goverman, J. Autoimmune T cell responses in the central nervous system. *Nat. Rev. Immunol.* **9**, 393–407 (2009).
12. Reynolds, J. M., Martinez, G. J., Chung, Y. & Dong, C. Toll-like receptor 4 signaling in T cells promotes autoimmune inflammation. *Proc. Natl Acad. Sci. USA* **109**, 13064–13069 (2012).
13. Heng, T. S. & Painter, M. W. The Immunological Genome Project: networks of gene expression in immune cells. *Nat. Immunol.* **9**, 1091–1094 (2008).
14. Papatheodorou, I. et al. Expression Atlas: gene and protein expression across multiple studies and organisms. *Nucleic Acids Res.* **46**, D246–D251 (2018).
15. Josefowicz, S. Z., Lu, L. F. & Rudensky, A. Y. Regulatory T cells: mechanisms of differentiation and function. *Annu. Rev. Immunol.* **30**, 531–564 (2012).
16. Kitagawa, Y. et al. Guidance of regulatory T cell development by Satb1-dependent super-enhancer establishment. *Nat. Immunol.* **18**, 173–183 (2017).
17. Lee, W. & Lee, G. R. Transcriptional regulation and development of regulatory T cells. *Exp. Mol. Med.* **50**, e456 (2018).
18. Luo, C. T. & Li, M. O. Transcriptional control of regulatory T cell development and function. *Trends Immunol.* **34**, 531–539 (2013).
19. Mottet, C., Uhlig, H. H. & Powrie, F. Cutting edge: cure of colitis by $CD4^+CD25^+$ regulatory T cells. *J. Immunol.* **170**, 3939–3943 (2003).
20. Wilson, J. E. et al. Inflammasome-independent role of AIM2 in suppressing colon tumorigenesis via DNA-PK and Akt. *Nat. Med.* **21**, 906–913 (2015).
21. Man, S. M. et al. Critical role for the DNA sensor AIM2 in stem cell proliferation and cancer. *Cell* **162**, 45–58 (2015).
22. Zeng, H. & Chi, H. mTOR signaling in the differentiation and function of regulatory and effector T cells. *Curr. Opin. Immunol.* **46**, 103–111 (2017).
23. Procaccini, C. et al. The proteomic landscape of human ex vivo regulatory and conventional T cells reveals specific metabolic requirements. *Immunity* **44**, 406–421 (2016).
24. Fragale, A. et al. IFN regulatory factor-1 negatively regulates $CD4^+$ $CD25^+$ regulatory T cell differentiation by repressing Foxp3 expression. *J. Immunol.* **181**, 1673–1682 (2008).
25. Overacre-Delgoffe, A. E. et al. Interferon-gamma drives T_{reg} fragility to promote anti-tumor immunity. *Cell* **169**, 1130–1141 (2017).
26. Wang, R. et al. The transcription factor Myc controls metabolic reprogramming upon T lymphocyte activation. *Immunity* **35**, 871–882 (2011).
27. Merkenschlager, M. & von Boehmer, H. PI3 kinase signalling blocks Foxp3 expression by sequestering Foxo factors. *J. Exp. Med.* **207**, 1347–1350 (2010).
28. Michalek, R. D. et al. Cutting edge: distinct glycolytic and lipid oxidative metabolic programs are essential for effector and regulatory $CD4^+$ T cell subsets. *J. Immunol.* **186**, 3299–3303 (2011).
29. Li, G. et al. EphB3 suppresses non-small-cell lung cancer metastasis via a PP2A/RACK1/Akt signalling complex. *Nat. Commun.* **3**, 667 (2012).
30. Apostolidis, S. A. et al. Phosphatase PP2A is requisite for the function of regulatory T cells. *Nat. Immunol.* **17**, 556–564 (2016).

Methods

Mice

All mice were housed and bred under specific pathogen–free conditions (temperature: 21–23 °C, humidity: 30–70%, 12-h light/dark cycle) in the animal facility at the University of North Carolina at Chapel Hill. All sex- and age- matched (9–12 weeks) mouse experiments were approved by Institution Animal Care and Use Committee of the University of North Carolina. We complied with all relevant ethical regulations. Wild-type (C57BL/6), *Aim2*$^{-/-}$, *Aim2*$^{+/+}$ FGC, *Aim2*$^{fl/fl}$ FGC, *Aim2*$^{+/+}$ FGC R26T, *Aim2*$^{fl/fl}$ FGC R26T, *Asc*$^{-/-}$, *Casp1*$^{-/-}$*Casp11*$^{-/-}$, *Rag1*$^{-/-}$, 2D2 (MOG_{35-55}-specific TCR transgenic), 2D2 × *Aim2*$^{-/-}$, *Tgfbr2*$^{fl/fl}$ *CD4-cre* (TGFbRII-KO), and CD45.1 congenic wild-type mice were generated on the C57BL/6 genetic background. *Aim2*$^{fl/fl}$ mice were generated using targeting vector (PRPGS00208_A_A10), which contained *loxP* sites flanking exon 7 and 12 of *Aim2*, purchased from Knock Out Mouse Project at Children's Hospital Oakland Research Institute, the University of California at Davis (KOMP-CHORI) repository, for insertion into C57BL/6N embryonic stem cells by the UNC Animal Models Core. Chimeras were obtained from implanted C57BL/6-albino females and backcrossed first to *Flpe*+ strain to remove neomycin selection marker and then to C57BL/6J for 7 generations plus sibling crosses to produce homozygous *flox/flox* lines. *Aim2*$^{fl/fl}$ mice were then crossed with FGC transgenic mice, in which a BAC transgenic construct encoding both enhanced green fluorescent protein (eGFP) and Cre under the control of *Foxp3* promoter was inserted into mouse genome[31], and *Rosa26*^{tdTomato} knock-in mice[32] (R26T; Jax Stock no. 007914) to generate T_{reg} cell-specific deletion of *Aim2* (*Aim2*$^{fl/fl}$ FGC or *Aim2*$^{fl/fl}$ FGC R26T) and control mice (*Aim2*$^{+/+}$ FGC or *Aim2*$^{+/+}$ FGC R26T). The sample sizes for all the mice experiments are determined based on the prevailing and widely accepted practice and similar designed experiments and results generated in the laboratory on the cellular immunology analyses. No statistical method was used to pre-determine sample size.

Experimental EAE

Sex- and age-matched (9 to 12 weeks old) wild-type and *Aim2*$^{-/-}$ mice were randomly allocated to be immunized subcutaneously (s.c.) with 200 μg of MOG_{35-55} peptide (MEVGWYRSPFSRVVHLYRNGK, GenemeSynthesis) emulsified in complete Freund's adjuvant (CFA) (Sigma) containing heat-killed *Mycobacterium tuberculosis* (Difco). In addition, the mice were administrated 200 ng of *Pertussis* toxin (List Biological Laboratories) intra-peritoneally (i.p.) on days 0 and 2. The severity of EAE was monitored and graded in a blinded fashion on a clinical score of 0 to 5: 0 = no clinical signs; 1 = limp tail; 2 = para-paresis (weakness, incomplete paralysis of one or two hind limbs); 3 = paraplegia (complete paralysis of two hind limbs); 4 = paraplegia with forelimb weakness or paralysis; 5 = moribund or death[33].

Flow cytometry and cell sorting

Lymphocytes were isolated from various lymphoid organs of age- and sex- matched mice of 8–12 weeks of age. Fluorescence-conjugated antibodies for CD4 (GK1.5), CD8 (53-6.7), CD45.1 (A20), CD45.2 (104), Vβ11 (RR3-15), CD25 (PC61.5), CD44 (IM7), CD62L (MEL-14), Ki67 (16A8), IFNγ (XMG1.2), IL-17A (TC11-18H10.1), IL-4 (11B11) and annexin V were purchased from Biolegend. BV421 mouse anti-AKT (pS473) (M89-61) and 7AAD were purchased from BD Bioscience. The anti-FOXP3 antibody (FJK-16 s) and Foxp3 staining kit (00-5523-00) were from eBioscience. For intracellular cytokine staining, lymphocytes were stimulated for 4 h with 50 ng ml^{-1} of phorbol 12-myristate 13-acetate (PMA) and 1 mM ionomycin in the presence of brefeldin A. Stained cells were analysed on L SRFortessa station or Canto (BD Biosciences) using FACSDiva software. A commercially available kit was used for intracellular cytokine staining in accordance with the manufacturer's protocol (BD Biosciences). For cell sorting, $CD4^+$ T cells or $CD25^+$ T_{reg} cells were enriched by MACS and then stained with fluorescence-conjugated antibodies. Stained cells were either acquired on LSRII or LSR Fortessa (BD biosciences) or sorted on the Moflow cell sorter (Dako cytomation, Beckman Coulter) by the Flow Core Facility of University of North Carolina at Chapel Hill. FACS data were analysed with FlowJo software (TreeStar). For the gating strategy for FACS analysis, see Supplementary Fig. 2.

$CD4^+$ T and T_{reg} cell adoptive transfer in EAE

Total lymphocytes were isolated from spleens and peripheral lymph nodes of wild-type and *Aim2*$^{-/-}$mice. Total $CD4^+$ T cells or $CD4^+CD25^+$ T_{reg} cells were enriched by MACS and Moflow cell sorter. $CD4^+$ T cells (5×10^6 per mouse) were introduced via retro-orbital injection into *Rag1*$^{-/-}$ female mice. One day later, the recipient mice were immunized with MOG_{35-55} to induce EAE as described above. To evaluate the function of T_{reg} cells in suppressing EAE, 2D2 $CD4^+$ T cells alone (5×10^5 per mouse), 2D2 $CD4^+$ T cells (5×10^5 per mouse) with wild-type or *Aim2*$^{-/-}$ T_{reg} cellss (2×10^5 per mouse) were transferred into *Rag1*$^{-/-}$ mice via retro-orbital injection. One day later, the recipient mice were immunized with MOG_{35-55} to induce EAE as described above.

$CD4^+CD45RB^{hi}$ T cell transfer colitis model

$CD4^+$ T cells from wild-type mice were enriched by anti-CD4 (L3T4) magnetic beads (Miltenyi Biotec) and stained with anti-CD4 Pacific Blue, anti-CD25 PE and anti-CD45RB FITC reagents. Naive CD4 ($CD4^+CD25^-CD45RB^{hi}$) T cells were sorted by FACS. T_{reg} cells ($CD4^+CD25^+$) of wild-type, *Aim2*$^{-/-}$ and *Asc*$^{-/-}$ mice were sorted by FACS. Approximately 5×10^5 naive T cells alone, or with 2×10^5 wild-type or *Aim2*$^{-/-}$ T_{reg} cells were transferred into *Rag1*$^{-/-}$ recipient mice by i.p. injection. The recipient mice were weighed twice every week to measure percentage of body weight change and major organs were collected for analysis at the end of experiment.

In vitro T cell activation, differentiation and proliferation

Lymphocytes were isolated from peripheral lymph nodes and spleens of age- and sex-matched mice and purified with CD4 microbeads (L3T4, Miltenyi Biotec). Purified $CD4^+$ T cells were cultured in RPMI 1640 medium containing 10% FBS, 1% penicillin-streptomycin and 2.6 μl of β-mercaptoethanol and activated with plate-coated 2.5 μg ml^{-1} anti-CD3 (145-2c11, BioXCell) and 1 μg ml^{-1} anti-CD28 (37.51, BioXCell) antibodies. For T_{reg} cell differentiation, designated doses of TGFβ (2 ng ml^{-1}) and IL-2 (40 U ml^{-1}) were added into the culture medium. Rapamycin and mTOR inhibitors (pp242) were used as indicated. For T_H1 cell differentiation, 20 ng ml^{-1} IL-12 (Biolegend) and 20 μg ml^{-1} anti-IL-4 (11B11, BioXcell) were added to the culture. For pathogenic T_H17 cell differentiation, 20 ng ml^{-1} IL-1β (Biolegend), 20 ng ml^{-1} IL-6 (Biolegend), 50 ng ml^{-1} IL-23 (Biolegend) and 10 μg ml^{-1} anti-IFNγ (XMG1.2, BioXcell) were added to the culture. For classical T_H17 cell differentiation, 1 ng ml^{-1} TGFβ (Biolegend), 40 ng ml^{-1} IL-6 (Biolegend) and 10 μg ml^{-1} anti-IFNγ (XMG1.2, BioXcell) were added to the culture. For CFSE proliferation assay, a final concentration of 2 μM of carboxyfluorescein succinimidyl ester (CFSE) (C1157, Life Technologies) was used to label $CD4^+$ T cells.

Ectopic expression of PP2A and RACK1 in T_{reg} cells

To generate the retrovirus expressing PP2A and RACK1, we first cloned PP2A (OriGene Technologies, MR204384L4) and RACK1 (OriGene Technologies, MR204575L3) into retroviral vectors MSCV-IRES-Thy1.1 (MIT, Addgene 17442) and MSCV-IRES-GFP (MIG, Addgene 20672) respectively, and generated MIT-PP2A and MIG-RACK1 retrovirus in 293T cells by transient transfection. For retroviral transduction, isolated $CD4^+$ T cells were stimulated with anti-CD3/CD28 in the presence of IL-2 (40 U ml^{-1}) and TGFβ (2 ng ml^{-1}) on day 0 and then transduced with indicated retroviruses containing 8 μg ml^{-1} polybrene (Sigma, H9268) by centrifuge at 1,500*g* at 30 °C for 1.5 h on day 1. Cells were collected and analysed by flow cytometry three days after retrovirus transduction.

In vitro T_{reg} cell suppression

T_{reg} cells (suppressor) from CD45.1.1 wild-type mice and CD45.2.2 *Aim2*$^{-/-}$ mice and naive CD4$^+$ T cells (responder) from CD45.1.2 wild-type young mice were sorted by FACS. To assess the efficacy of T_{reg} cell-mediated immune suppression in vitro, 1×10^5 sorted responder T cells were labelled with CFSE and mixed with varying amounts (as indicated) of T_{reg} suppressor cells. Cell mixtures were stimulated with soluble CD3 antibody (0.125 μg ml^{-1}) in the presence of 4×10^5 irradiated (3,000 cGy) T cell-depleted splenocytes as antigen-presenting cells. The proliferation of responder cells was assessed by CFSE dilution detected by flow cytometric analysis 72 h after stimulation.

Histology

For the assessment of tissue pathology, following an initial perfusion with PBS, mice were subsequently perfused trans-cardially with 4% paraformaldehyde and spinal cords were removed. Tissues were processed and blocked in paraffin wax. Transverse sections of the lumber spinal cord were stained with haematoxylin and eosin (H&E) or Luxol Fast Blue and periodic acid-Schiff (LFB-PAS). The number of inflammatory foci and total demyelination were measured using methods described previously[34]. In brief, the numbers of inflammatory foci that contained at least 20 cells were counted within each H&E-stained section in a blinded fashion. Estimates were made of the number of foci, when foci coalesced. Areas of demyelination were assessed in LFB-PAS–stained sections. ImageJ software was used to manually trace the total cross-sectional area and the demyelinated area of each section. Total demyelination was expressed as a percentage of the total spinal cord area[34]. Colons were Swiss rolled, fixed in 10% neutral-buffered formalin and routinely paraffin embedded and processed. Five micrometre-thick colon sections were stained with H&E and evaluated by a board-certified veterinary pathologist (A.B.R.) in a blinded manner to perform semi-quantitatively scoring of histopathology. Histology scores represented the sum of each histological alterations as outlined here: inflammation, epithelial defects, area of inflammation, area of epithelial defect, crypt atrophy and dysplasia-neoplasia, by giving each parameter a separate score (0–4) for severity and extent as previously described[35].

Enzyme-linked immunosorbent assay

Both spinal cord homogenates and colon-secreted cytokines were analysed by enzyme-linked immunosorbent assay (ELISA, MCS00, R&D Systems, or by multiplex analyte assay using Luminex technology (EMD Millipore) according to manufacturers' protocols. IL-18 (Invitrogen BMS618-3), IL-6 (R&D DY406) and TNFα (Biolegend 430904) were measured using ELISA assays according to manufacturer's instructions. For colon-secreted cytokines, excised colons were washed and flushed with PBS containing 2 × penicillin/streptomycin. The distal-most 1 cm^2 colon sections were cultured for 15 h in RPMI medium containing 2 × penicillin/streptomycin at 37 °C. Supernatants were collected, cleared of debris by centrifugation and assessed for cytokines by Luminex analyses.

Immunoblotting, immunoprecipitation and mass spectrometry

CD4$^+$CD25$^+$ T_{reg}, TGFβ-induced T_{reg}, CD4$^+$ T and CD8$^+$ T cells were lysed in RIPA buffer supplemented with complete proteinase inhibitor cocktail and PhoSTOP phosphatase inhibitors. Protein lysates were cleared of insoluble material through centrifugation and the resulting protein lysates were treated with sample buffer and subjected to SDS–PAGE. In brief, total proteins were wet transferred to 0.2 μm nitrocellulose membranes (BioRad Laboratories), which were blocked using 5% BSA in 1 × TBS-T buffer for 1 h at room temperature. The membranes were incubated overnight using the following primary antibodies from Cell Signaling Technology (CST): anti-p-AKT (Ser473) (cat. no. 4060) (WB, 1:1,000), anti-AKT (cat. no. 9272) (WB, 1:1,000), anti-p-FOXO1/3A (cat. no. 9464) (WB, 1:1,000), anti-p-4E-BP1 (cat. no. 2855) (WB, 1:1,000), anti-p-S6 (Ser235/236) (cat. no. 4856) (WB, 1:1,000), anti-MYC (cat. no. 5605) (WB, 1:1,000), anti-p-STAT1 (Tyr 701) (cat. no. 9167), (WB, 1:1,000) anti-AIM2 (cat.no. 63660) (WB, 1:1,000) and anti-PP2A catalytic subunit (cat. no. 2259) (WB, 1:1,000). The anti-RACK1 (sc-17754) (WB, 1:1,000) and anti-actin HRP (sc-4778) (WB, 1:5,000) reagents were from Santa Cruz Bioteconology. Membranes were washed in TBS-T and incubated with the following appropriate secondary antibodies from Jackson ImmunoResearch Laboratories: mouse anti-rabbit-HRP, light chain-specific (211-032-171) (WB, 1:10,000), and donkey anti-mouse HRP (715-035-151) (WB, 1:10,000). Protein bands were visualized following exposure of the membranes to ECL substrate solution (ThermoFisher) and quantified by densitometric analysis using Image Lab software. For gel source data, see Supplementary Fig. 1.

For immunoprecipitation, wild-type and *Aim2*$^{-/-}$ CD4$^+$ T cells differentiated under T_{reg} cell polarizing and natural (IL-2 only) conditions for 24 h were lysed with CHAPS lysis buffer (50 mM Tris HCl, pH 7.4, 120 mM NaCl, 0.3% CHAPS) and sonicated with Bioruptor PICO. Cell lysates were incubated with 50 μl magnetic protein A/G beads (Bio-Rad) conjugated with anti-AIM2 (CST, cat. no. 63660) (IP, 1:200) or anti-RACK1 (CST, cat. no. 5432 s) (IP, 1:200) antibodies treated by dimethyl pimelimidate. After overnight incubation, beads were washed four times with lysis buffer. Associated protein was eluted by Laemmli sample buffer (Bio-Rad) and incubated at 9 5 °C for 5 min. Eluted samples were separated by SDS–PAGE gel and analysed by immuno-blotting.

For mass spectrometry analysis, anti-AIM2 antibody immunoprecipitated proteins were eluted with buffer containing 8 M urea, 50 mM Tris (pH 8.0), reduced with 5 mM DTT and alkylated with 15 mM iodoacetamide. Trypsin digestion was performed at room temperature overnight in 2 M urea buffer. The peptides were desalted on C18 stage-tips and dissolved in 0.1% formic acid. Peptides were loaded on an Acclain PepMap RSLC C18 Column (150 mm × 75 μm ID, C18, 2 μm, Thermo Fisher Scientific) and analysed on a Q-Exactive HF-X coupled with Easy nanoLC 1200 (Thermo Fisher Scientific). Analytical separation of all tryptic peptides was achieved with a linear gradient of 5–30% buffer B over 29 min, 30–45% B over 6 min followed a ramp to 100% B in 1 min and 9 min wash periods with 100% buffer B, where buffer A was aqueous 0.1% formic acid and buffer B contained 80% acetonitrile and 0.1% formic acid. Liquid chromatography–mass spectrometry (LC–MS) experiments were performed in a data-dependent mode with full MS (externally calibrated to a mass accuracy of <5 ppm and a resolution of 60,000 at m/z 200) followed by high energy collision-activated dissociation-MS/MS of the top 15 most intense ions with a resolution of 15,000 at m/z 200. High energy collision-activated dissociation-MS/MS was used to dissociate peptides at a normalized collision energy (NCE) of 27 eV. Dynamic exclusion with 20.0 s was enabled. Then the mass spectra were processed and peptide identification was performed using the Andromeda search engine found in MaxQuant software version 1.6.0.16 (Max Planck Institute, Germany) against the UniProt mouse protein sequence database (UP000000589). Peptides were identified with a target-decoy approach using a combined database consisting of reverse protein sequences of the database. Up to two missed cleavages was allowed. Peptide identifications were reported by filtering reverse and contaminant entries and assigning to leading razor protein. Peptide inference and protein identification were filtered to maximum 1% and 1% false discovery rate, respectively. Data processing and statistical analysis were performed on Perseus (Version 1.6.0.7). A two sample t-test statistics was used with a $P < 0.05$ to report statistically significant expression.

Glycolytic and mitochondrial respiration rate measurement

The ECAR and OCR were measured using the Seahorse Extracellular flux XF24e (Agilent) according to industry manuals. CD4$^+$CD25$^+$ T_{reg} cells were isolated from wild-type and *Aim2*$^{-/-}$ mice and then stimulated with anti-CD3/CD28 and IL-2 (500 U ml^{-1}) for 24 h. For in vitro TGFβ-promoted T_{reg} cells, wild-type and *Aim2*$^{-/-}$ CD4$^+$ T cells were

stimulated with anti-CD3/CD28 in the presence of TGFβ (2 ng ml^{-1}) and IL-2 (40 U ml^{-1}) for 48 h. Before metabolic flux analysis, T_{reg} cells were seeded at a density of 5×10^5 cells per well. ECAR profiles were assessed by real-time measurements at basal condition and after the addition of 10 mM glucose, 1 μM oligomycin and 20 mM 2-deoxyglucose (2-DG).

OCR profiles were assessed by real-time measurements at basal condition and after the addition of 1 μM oligomycin (75351), 4 μM FCCP (C2920), and 1 μM rotenone (R8875), and all the reagents are from Sigma-Aldrich. Fatty acid oxidation assay was performed where cells were starved in substrate-limited medium and given only BSA or palmitate-BSA (cat no. 102720-100) in fatty acid oxidation assay medium. Then OCR was measured to indicate oxidation of fatty acids according to the Agilent fatty acid oxidation assay manual.

RNA preparation and quantitative PCR

Total RNA was prepared from T cells using TRIzol reagent (Invitrogen) per manufacturer's instructions and was reverse-transcribed into cDNA with iScript cDNA Synthesis Kit (Bio-Rad, cat. no. 1708891). The Taqman probes were purchased from Applied Biosystems and quantitative PCR was performed on the ABI9700 real-time PCR system with QuantStudio software (Applied Biosystems).

RNA-seq

For RNA-seq analysis, total RNA was extracted from T_{reg} cells using the Direct-zol miniprep kit (Zymo Research, R2060). The RNA samples were first enriched by Oligo(dT) magnetic beads and used to construct BGISEQ-500 libraries. RNA-seq libraries were sequenced using the 50 bp single-end protocol (in vivo isolated T_{reg} cells) or 100 bp paired-end protocol (TGFβ-induced T_{reg} cells) via the BGISEQ-500 sequencer per manufacturer's protocol. After filtering of adaptors and low quality reads, clean reads (>26 million reads per sample for in vivo isolated T_{reg} cells and >40 million reads per sample for TGFβ-induced T_{reg} cells) were mapped to the mouse reference genome using HISAT/Bowtie2 tool. Mapping results were stored in BAM files using SAMtools.

Total read counts at the gene level were summarized using featureCounts function in the Rsubread[36] in R environment, with the R package biomaRt for gene and transcript mapping. The differential expression genes were analysed by DESeq2 package[37] with default settings using total read counts as input and the adjusted *P* value (padj) less than 0.05. Heat maps of gene expression were generated based on zscore values of normalized expression matrix from DESeq2 analysis in Gene-E from Broad Institute (www.broadinstitute.org/GENE-E/).

GSEA

GSEA[38] was performed using the Java application available from The Broad Institute (www.broadinstitute.org/gsea/). Gene set databases including Hallmarks (h.all.v6.1.symbols.gmt), KEGG (c2.cp.kegg.v6.1.symbols.gmt) and Reactome (c2.cp.reactome.v6.1.symbols.gmt) from the Molecular Signatures Database (MSigDB)[39] were used in the analysis. One thousand gene set permutations were performed. An FDR cutoff of <0.05 was used for enriched terms, as is recommended when performing permutations by gene set. R version 3.5.0 was used.

Statistical analysis

Data analysis was processed and represented by Prism (GraphPad, San Diego). Statistical significance was determined by two-sided Student's *t*-test, two-way ANOVA followed by Tukey test or Holm–Sidak's multiple-comparisons tests indicated in figures. A *P* value of less than 0.05 (confidence interval of 95%) was considered significant. $^*P < 0.05$, $^{**}P < 0.01$, $^{***}P < 0.001$ and $^{****}P < 0.0001$. The exact *P* values are shown in the source data. The sample sizes are stated in the figure legends to indicate biologically independent replicates used for statistical analyses.

Reporting summary

Further information on research design is available in the Nature Research Reporting Summary linked to this paper.

Data availability

The RNA-seq data are available in the Gene Expression Omnibus (GEO) repository at the National Center for Biotechnology Information under accession number GSE133019. The MS proteomics data have been deposited to the ProteomeXchange Consortium via the PRIDE partner repository with the dataset identifier PXD018638. All other data supporting the findings of this study are available from the corresponding authors upon reasonable request. Source data are provided with this paper.

31. Zhou, X. et al. Selective miRNA disruption in T_{reg} cells leads to uncontrolled autoimmunity. *J. Exp. Med*. **205**, 1983–1991 (2008).
32. Madisen, L. et al. A robust and high-throughput Cre reporting and characterization system for the whole mouse brain. *Nat. Neurosci*. **13**, 133–140 (2010).
33. Miller, S. D. & Karpus, W. J. Experimental autoimmune encephalomyelitis in the mouse. *Curr. Protoc. Immunol*. **77**, 15.1.1–15.1.18 (2007).
34. Matsushita, T., Yanaba, K., Bouaziz, J. D., Fujimoto, M. & Tedder, T. F. Regulatory B cells inhibit EAE initiation in mice while other B cells promote disease progression. *J. Clin. Invest*. **118**, 3420–3430 (2008).
35. Erben, U. et al. A guide to histomorphological evaluation of intestinal inflammation in mouse models. *Int. J. Clin. Exp. Pathol*. **7**, 4557–4576 (2014).
36. Liao, Y., Smyth, G. K. & Shi, W. The Subread aligner: fast, accurate and scalable read mapping by seed-and-vote. *Nucleic Acids Res*. **41**, e108 (2013).
37. Love, M. I., Huber, W. & Anders, S. Moderated estimation of fold change and dispersion for RNA-seq data with DESeq2. *Genome Biol*. **15**, 550 (2014).
38. Subramanian, A. et al. Gene set enrichment analysis: a knowledge-based approach for interpreting genome-wide expression profiles. *Proc. Natl Acad. Sci. USA* **102**, 15545–15550 (2005).
39. Liberzon, A. et al. Molecular signatures database (MSigDB) 3.0. *Bioinformatics* **27**, 1739–1740 (2011).

Acknowledgements The following funding supports are acknowledged: NIH (AI029564, CA156330, DK094779, AI097392, AI123193), the National Multiple Sclerosis Society (CA10068 to J.P.-Y.T. and FG 1968-A-1 to W.C.), NIAID (AI067798 to J.P.-Y.T., H.G. and W.J.B.), the National Multiple Sclerosis Society (RG-1802-30483), and a Yang Family Biomedical Scholars Award to Y.Y.W. We received help from G.D. Sempowski (Duke University, Duke Human Vaccine Institute, Durham, NC, USA, Immune Monitoring Core for AI067798) for the Luminex assay and analysis. We thank B. Sartor (P01-DK094779) for advice regarding the colitis model, N. Fisher and J. Dow (UNC flow cytometry facility supported in part by P30 CA016086 Cancer Center Core Support Grant) for cell sorting, and Dale Cowley (UNC Animal Models Core for P30 CA016086) for generating *Aim2*$^{fl/fl}$ mice. This work benefitted from a publicly available online database assembled by the ImmGen consortium and The European Bioinformatics Institute (EMBL-EBI) without prior permission. We thank E. Holley-Guthrie for genotyping mice.

Author contributions W.C. and Z.G. contributed equally to this manuscript. W.C., Z.G., Y.Y.W. and J.P.-Y.T. designed experiments and wrote the manuscript. W.C. and Z.G. performed and analysed most of the experiments. H.G., L.C. and G.Z. contributed to the colitis experiments. K.L. and M.D. contributed to the western blots. L.X. and X.C. contributed to IP–MS analysis. S.A.G. contributed to quantitative PCR analysis. X.T. contributed to bioinformatics analysis. E.R. contributed to the metabolism assays. Y.W. and M.A.S. contributed to the scoring and quantitation of spinal cord pathology. S.A.M. contributed to the scoring of colon pathology. W.J.B., L.F. and S.Z. assisted in the mouse experiments. W.J.B. edited the manuscript.

Competing interests The authors declare no competing interests.

Additional information

Supplementary information The online version contains supplementary material available at https://doi.org/10.1038/s41586-021-03231-w.

Correspondence and requests for materials should be addressed to Y.Y.W. or J.P.-Y.T.

Peer review information *Nature* thanks Kate Schroder and the other, anonymous, reviewer(s) for their contribution to the peer review of this work.

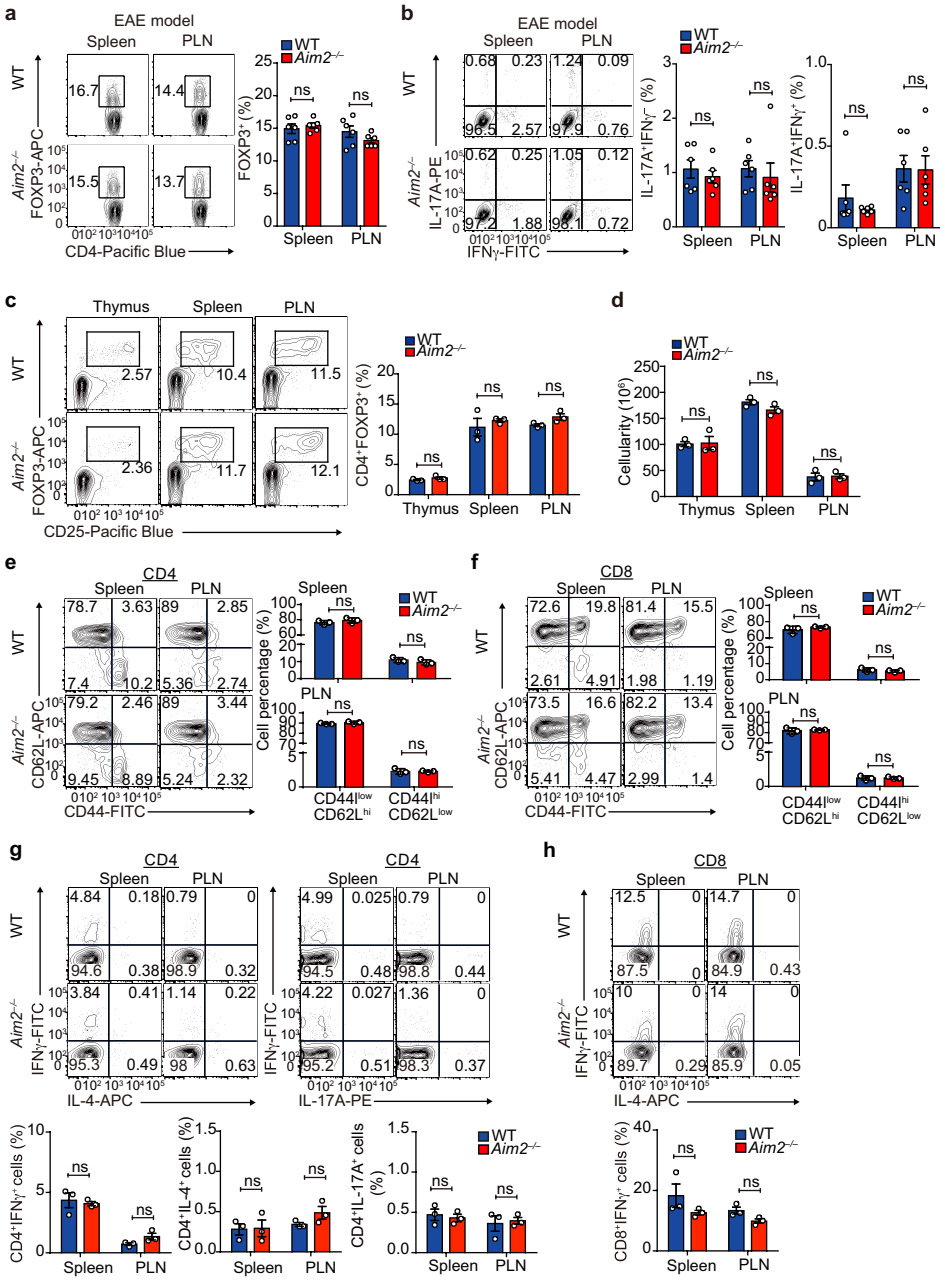

Extended Data Fig. 1 | *Aim2*$^{-/-}$ mice show normal T cell homeostasis. **a**, **b**, Flow cytometry of CD4$^+$FOXP3$^+$ T_{reg} cells (**a**) and IFNγ-, IL-17A-producing CD4$^+$ T cells (**b**) in the spleen and PLN of wild-type and *Aim2*$^{-/-}$ mice at day 14 of an EAE course. Representative results (left) and statistical analysis (right) of six experiments are shown. **c**, Flow cytometry of CD4$^+$FOXP3$^+$ T_{reg} cells in the thymus, spleen and PLN of wild-type and *Aim2*$^{-/-}$ mice. Representative results (left) and statistical analysis (right) of three experiments are shown. **d**, Total number of cells isolated from the thymus, spleen and PLN of wild-type and *Aim2*$^{-/-}$ mice. Experimental design and statistical analysis performed as described in **c**. **e**, **f**, Flow cytometry of naive, effector/memory CD4$^+$ (**e**) and CD8$^+$ (**f**) T cells in the spleen and PLN of wild-type and *Aim2*$^{-/-}$ mice ($n = 3$ per group) analysed by CD44 and CD62L expression. Experimental design and statistical analysis performed as described in **c**. **g**, **h**, Flow cytometry of IFNγ-, IL-4- or IL-17A-producing CD4$^+$ cells (**g**) and IFNγ-producing CD8$^+$ T cells (**h**) in wild-type and *Aim2*$^{-/-}$ mice ($n = 3$ per group). Experimental design and statistical analysis performed as described in **c**. Representative (top) and composite (bottom) data are shown. Data are mean ± s.e.m. *P* values determined by two-sided *t*-test. ns, not significant.

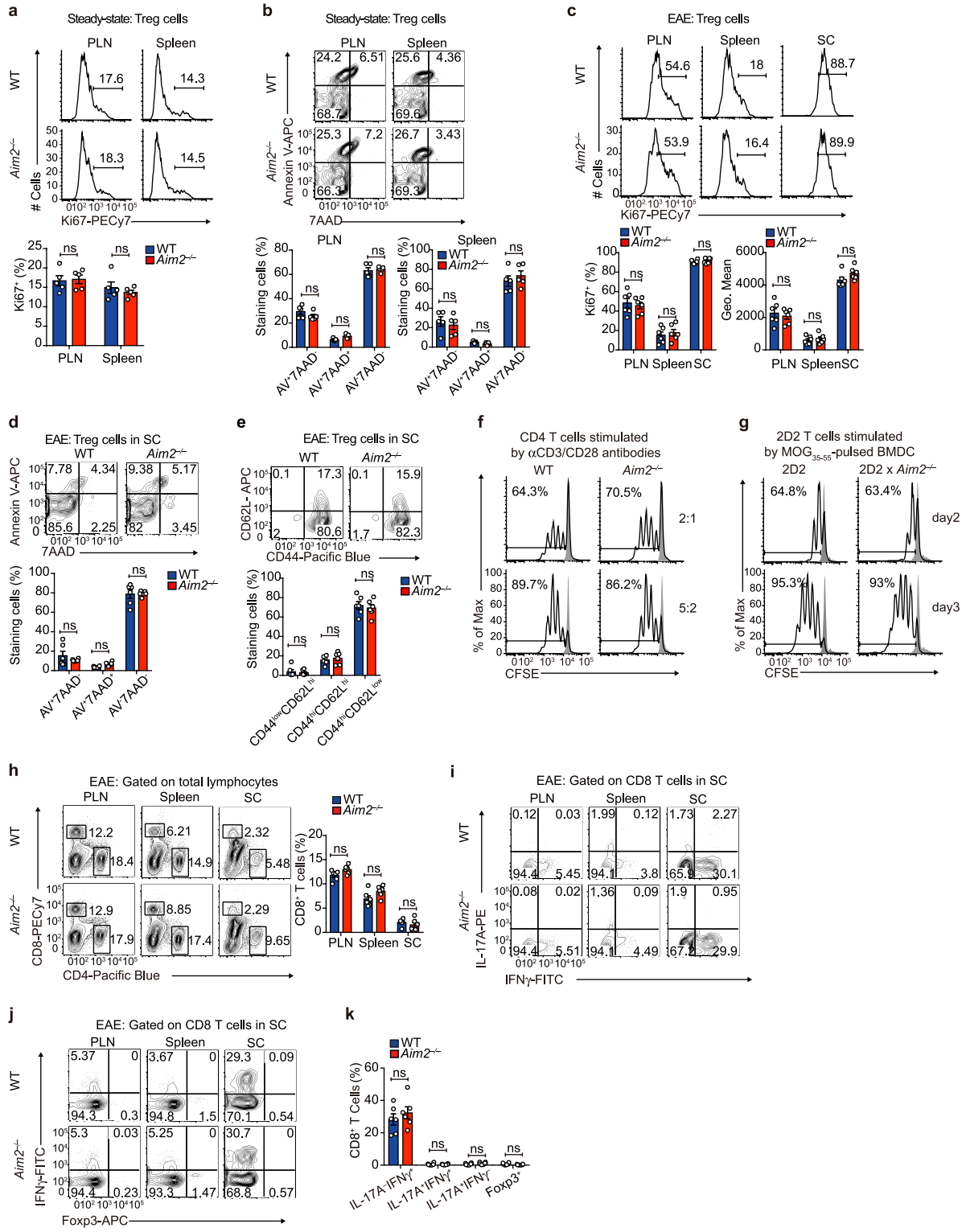

Extended Data Fig. 2 | See next page for caption.

Extended Data Fig. 2 | *Aim2*$^{-/-}$ mice show normal T_{reg} cell proliferation, survival and ratio of central or effector T_{reg} cells at steady state or during EAE in vivo, normal CD4$^+$ T cell proliferation in vitro, and normal CD8$^+$ T cell distribution and cytokine production during EAE. a, Flow cytometry of Ki67 to analyse proliferation of wild-type and *Aim2*$^{-/-}$ T_{reg} cells in the PLN and spleen at steady state. Representative results (top) and statistical analysis (bottom) of five experiments are shown. **b**, Apoptosis of wild-type and *Aim2*$^{-/-}$ T_{reg} cells in the PLN and spleen at steady state was analysed by flow cytometry using annexin V and 7-aminoactinomycin D (7AAD) staining. Representative results (top) and statistical analysis (bottom) of five experiments are shown. **c**, Flow cytometry of Ki67 to analyse proliferation of wild-type and *Aim2*$^{-/-}$ T_{reg} cells in the PLN, spleen and spinal cord during EAE. Representative results (top) and statistical analysis (bottom) of six experiments are shown. **d**, Apoptosis of wild-type and *Aim2*$^{-/-}$ T_{reg} cells in spinal cord during EAE was analysed by flow cytometry using annexin V and 7AAD staining. Representative results (top) and statistical analysis (bottom) of six experiments are shown. **e**, Flow cytometry of CD44 and CD62L in wild-type and *Aim2*$^{-/-}$ T_{reg} cells isolated from spinal during EAE. Representative results (top) and statistical analysis (bottom) of six experiments are shown. **f**, Flow cytometry of wild-type and *Aim2*$^{-/-}$ CD4$^+$ T cell proliferation stimulated with different doses of anti-CD3/CD28, determined by CFSE dilution assay. Representative results of two independent experiments. **g**, Flow cytometry of 2D2 and *Aim2*-deficient 2D2 (2D2 × *Aim2*$^{-/-}$ CD4$^+$ T cell proliferation stimulated with bone marrow-derived dendritic cells (BMDCs) pulsed with MOG_{35-55} peptide) as determined by CFSE dilution assay. Representative of two independent experiments. **h**, Flow cytometry of wild-type and *Aim2*$^{-/-}$ CD4$^+$ or CD8$^+$ T cells in the PLN, spleen and spinal cord during EAE. Representative results (left) and statistical analysis (right) of six experiments are shown. **i**–**k**, Flow cytometry of IFNγ-, IL-17A-producing (**i**) or FOXP3$^+$, IFNγ-producing (**j**) CD8$^+$ T cells in the PLN, spleen and spinal cord during EAE. Representative results (**i**, **j**) and statistical analysis (**k**) of six experiments are shown. Data are mean ± s.e.m. *P* values determined by two-sided *t*-test.

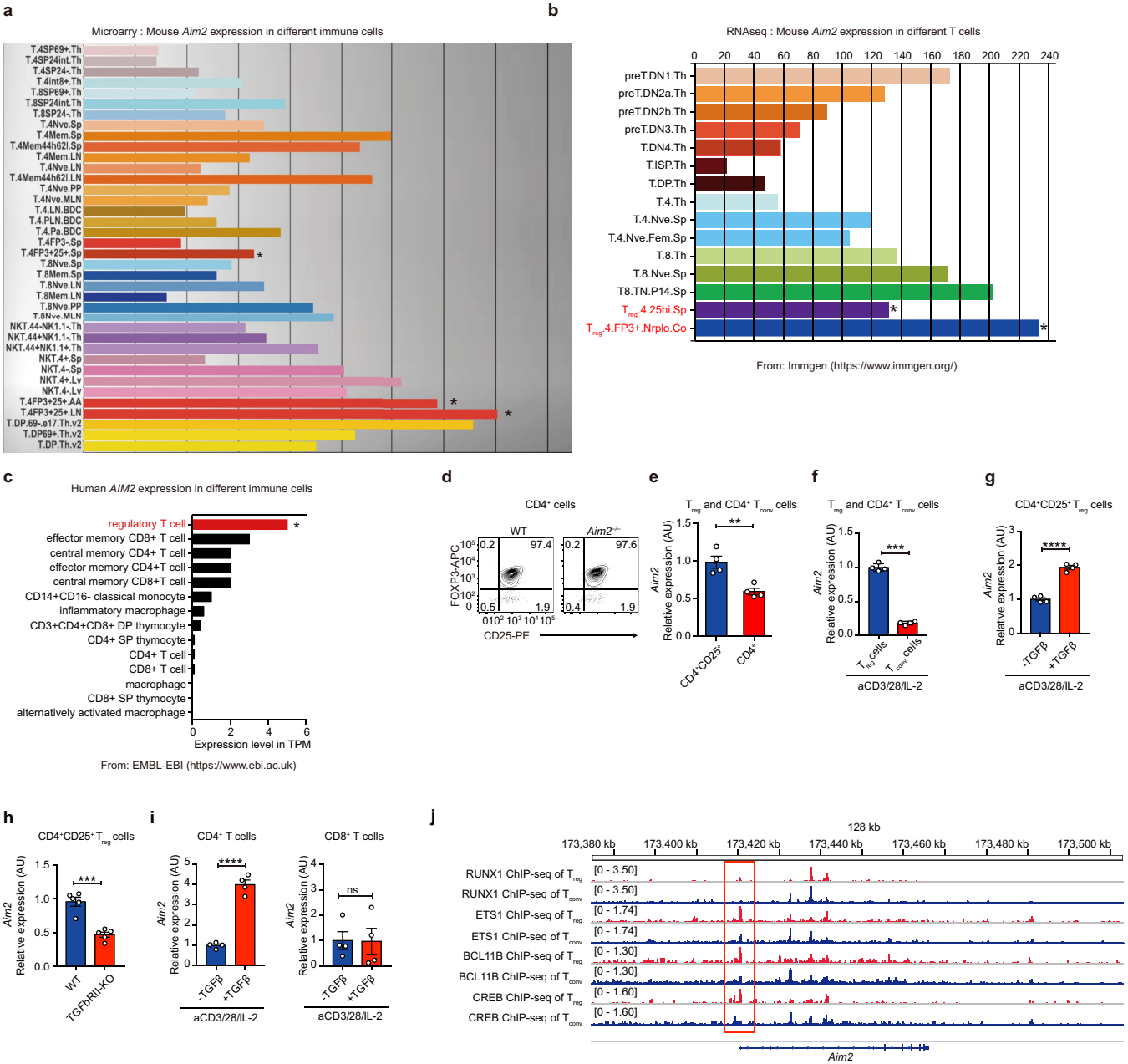

Extended Data Fig. 3 | *Aim2* is highly expressed in T_{reg} cells and its promoter is bound by T_{reg} cell-related transcription factors. a, **b**, Mouse *Aim2* gene expression in different T cell subsets from publicly available gene microarray (**a**) and RNA-seq (**b**) databases (https://www.immgen.org/). **c**, Human *AIM2* gene expression in T cell and macrophage subsets from the Expression Atlas of EMBL-EBI (https://www.ebi.ac.uk/). **d**, Purity of isolated $CD4^+CD25^+$ T_{reg} cells from wild-type and *Aim2*$^{-/-}$ mice. Flow cytometry of $CD4^+CD25^+FOXP3^+$ T_{reg} cells shows that more than 97% of isolated T_{reg} cells are $FOXP3^+$ cells. **e**, *Aim2* expression was assessed from isolated $CD4^+CD25^+$ T_{reg} cells and $CD4^+$ T cells. Cells were freshly isolated from pooled spleens and lymph nodes and purified by MACS beads. *Aim2* mRNA expression was examined by quantitative PCR; $n = 4$ experiments. **f**, The mRNA expression of *Aim2* in T_{reg} cells and $CD4^+$ T cells stimulated with anti-CD3/CD28 plus IL-2 (500 U ml^{-1}) for 24 h; $n = 4$ experiments. **g**, The mRNA expression of *Aim2* in T_{reg} cells stimulated with anti-CD3/CD28 plus IL-2 (500 U ml^{-1}) in the absence (–) or presence (+) of TGFβ (1 ng ml^{-1}) for 24 h; $n = 4$ experiments. **h**, *Aim2* expression was assessed in freshly isolated $CD4^+CD25^+$ T_{reg} cells from wild-type and *Tgfbr2*$^{fl/fl}$ *CD4-cre* (TGFbRII-KO) mice. *Aim2* mRNA expression was examined by quantitative PCR; $n = 5$ experiments. **i**, The mRNA expression of *Aim2* in naive $CD4^+$ or $CD8^+$ T cells stimulated with anti-CD3/CD28 plus IL-2 (40 U ml^{-1}) in the absence or presence of TGFβ (1 ng ml^{-1}) for 24 h; $n = 4$ experiments. **j**, ChIP–seq analysis of RUNX1, ETS1, BCL11B and CREB binding to the *Aim2* promoter region in T_{reg} cells and $CD4^+$ T_{conv} cells (NCBI SRA database number: DRP003376). Data are mean ± s.e.m. $^{**}P < 0.01$, $^{***}P < 0.001$, $^{****}P < 0.0001$, two-sided *t*-test.

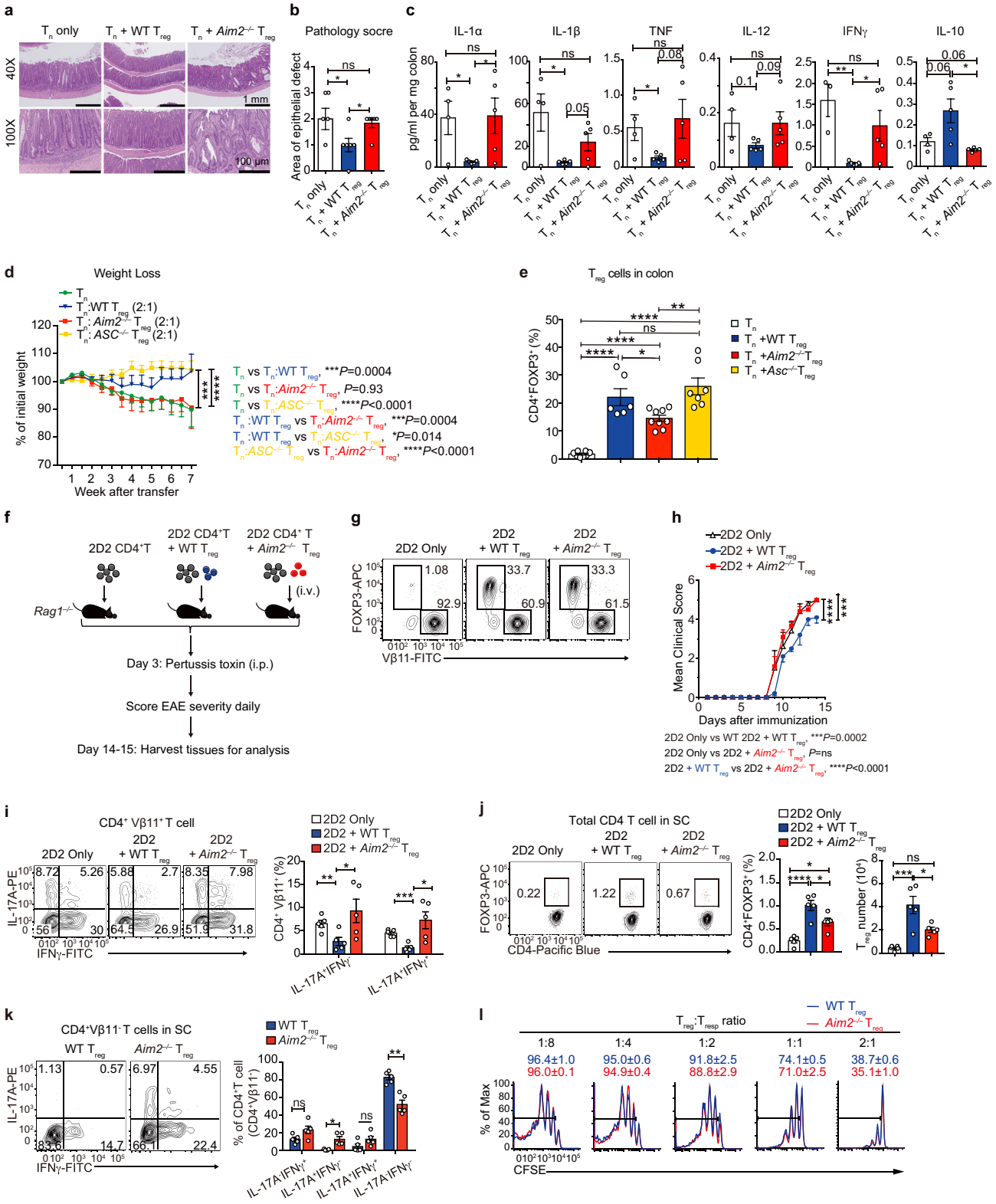

Extended Data Fig. 4 | See next page for caption.

Extended Data Fig. 4 | AIM2 is essential for T_{reg} cells to suppress T cell-mediated colitis and EAE. a, Haematoxylin and eosin (H&E) staining of colons from T cell-induced colitis mice transferred with wild-type $CD4^+CD45RB^{hi}$ T cells (T_n) alone ($n = 5$) or in combination with wild-type ($n = 6$) or *Aim2*$^{-/-}$ ($n = 6$) $CD4^+CD25^+$ T_{reg} cells, collected 7 weeks after T cell transfer. Scale bars, 1 mm (40×) and 100 µm (100×). **b**, Statistical analysis of pathology score of colitis mice with biological replicates of each group depicted in **a**. T_n only: $n = 5$; T_n + WT T_{reg}: $n = 6$; T_n + *Aim2*$^{-/-}$ T_{reg}: $n = 6$. **c**, Cytokine levels in the supernatants of colon tissue cultures from mice depicted in **a** measured by Millipore Luminex assay, collected 7 weeks after T cell transfer. T_n only: $n = 4$; T_n + WT T_{reg}: $n = 5$; T_n+*Aim2*$^{-/-}$ T_{reg}: $n = 5$. **d**, Change of body weight of *Rag1*$^{-/-}$ recipients receiving wild-type naive $CD4^+CD45RB^{hi}$ T cells (T_n) alone or in combination with wild-type, *Aim2*$^{-/-}$ or *Asc*$^{-/-}$ $CD4^+CD25^+$ T_{reg} cells. *Rag1*$^{-/-}$ recipients of T_n ($n = 8$), T_n + WT T_{reg} ($n = 6$), T_n + *Aim2*$^{-/-}$ T_{reg} ($n = 9$), T_n + *Asc*$^{-/-}$ T_{reg} ($n = 7$); composite of two independent experiments. *P* value determined by two-way ANOVA. **e**, Flow cytometry of $CD4^+FOXP3^+$ T_{reg} cells in the colons of *Rag1*$^{-/-}$ recipients of T_n ($n = 8$), T_n + WT T_{reg} ($n = 6$), T_n + *Aim2*$^{-/-}$ T_{reg} ($n = 9$), T_n + *Asc*$^{-/-}$ T_{reg} ($n = 7$), collected 7 weeks after T cell transfer. *P* value by one-way ANOVA with Tukey's multiple comparisons test. **f**, Schema of EAE induction in *Rag1*$^{-/-}$ mice transferred with 2D2 $CD4^+$ T cells either alone or in combination with wild-type or *Aim2*$^{-/-}$ $CD4^+CD25^+$ T_{reg} cells. Lymphocytes and tissues were obtained 14–15 days after initial T cell transfer for further analysis. **g**, Flow cytometry shows the distributions of 2D2 $CD4^+$ T cells ($V\beta11^+$) or T_{reg} cells ($FOXP3^+$) before transfer to *Rag1*$^{-/-}$ recipient mice. **h**, Mean EAE clinical score of mice depicted in **f**; $n = 5$ mice per group. *P* value by two-way ANOVA and Holm–Sidak post hoc test. Data are representative of three independent experiments. The difference between 2D2 alone and 2D2 with *Aim2*$^{-/-}$ T_{reg} cells is not significant. **i**, Flow cytometry of $IFN\gamma^+$ or $IL\text{-}17A^+$ $CD4^+V\beta11^+$ T cells in spinal cords from groups depicted in **f**. Left, representative sample; right, composite data pooled of five mice per group from three independent experiments. **j**, Flow cytometry of $CD4^+FOXP3^+$ T_{reg} cells from spinal cord derived from mice depicted in **f**. Left, representative sample; right, composite data pooled of five mice per group from three independent experiments. *P* value determined by one-way ANOVA with Tukey's multiple comparisons test. **k**, Flow cytometry of $IFN\gamma^+$ or $IL\text{-}17A^+CD4^+V\beta11^-$ T cells in spinal cord from groups depicted in **f**. Left, representative sample; right, composite data summarized from five biological replicates. **l**, $CD25^-CD44^{low}CD62L^{hi}$ naive $CD4^+$ T cells (T_{resp} cells) were isolated from wild-type mice and labelled with CFSE. $CD4^+CD25^+$ T_{reg} cells were isolated from wild-type or *Aim2*$^{-/-}$ mice by FACS. T_{resp} and T_{reg} cells of different genotypes were mixed at indicated ratios and stimulated with anti-CD3 in the presence of irradiated antigen-presenting cells from mixed spleens and lymph nodes. The suppressive activity of T_{reg} cells was assessed by CFSE dilution of T_{resp} cells. Data are mean ± s.e.m. $^*P < 0.05$, $^{**}P < 0.01$, $^{***}P < 0.001$, $^{****}P < 0.0001$, two-sided *t* test unless specified.

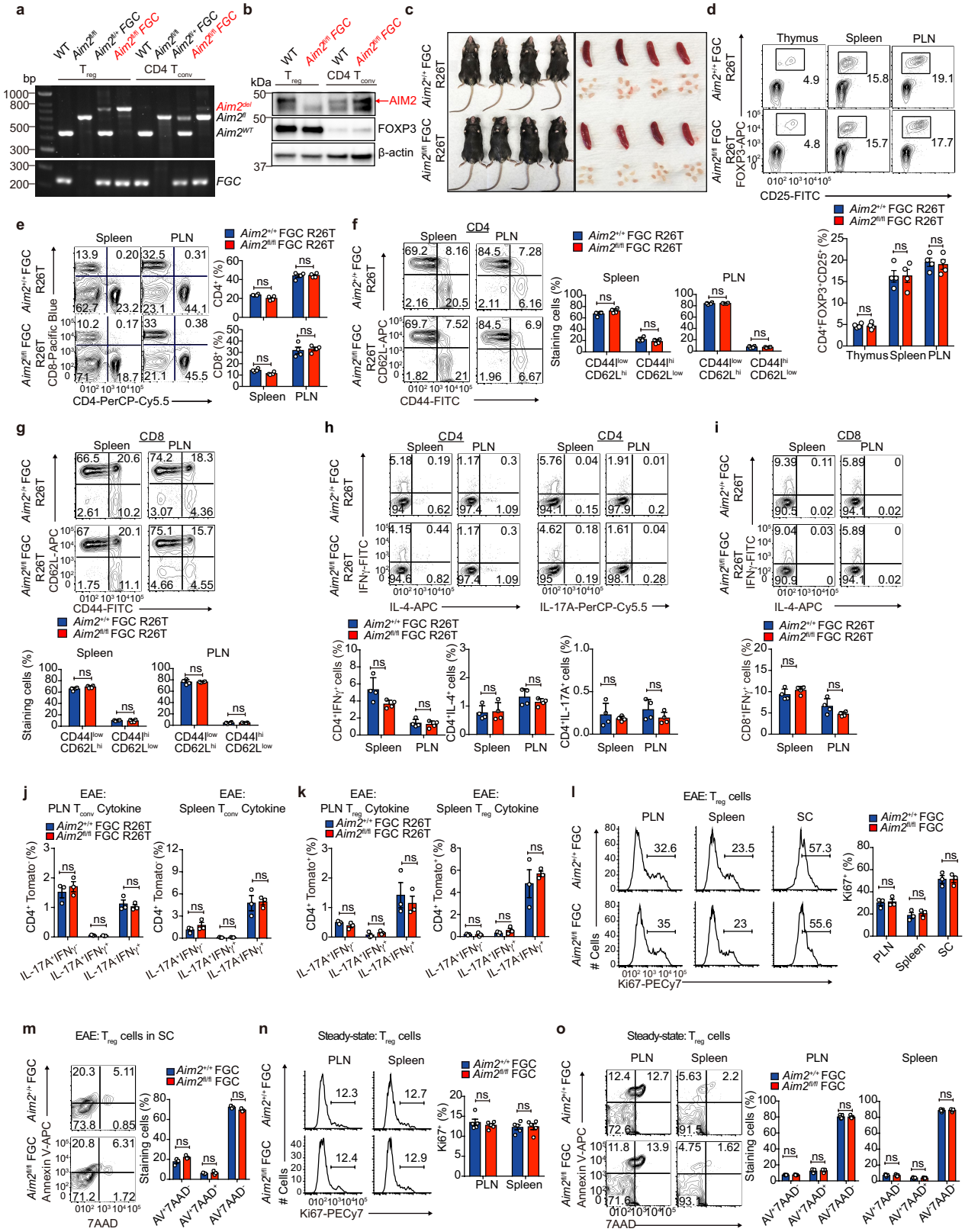

Extended Data Fig. 5 | See next page for caption.

Extended Data Fig. 5 | *Aim2*$^{fl/fl}$ FGC R26T mice show normal T cell homeostasis, normal T_{reg} cell proliferation and survival at steady state and during EAE. a, Genotyping of FACS-sorted T_{reg} ($CD4^+CD25^+GFP^+$) and $CD4^+$ T_{conv} ($CD4^+CD25^-$) cells showing efficient deletion of *Aim2* genomic DNA in T_{reg} cells. The image is representative of three independent experiments. **b**, Immunoblot analysis of AIM2 protein in T_{reg} cells from *Aim2*$^{+/+}$ FGC R26T and *Aim2*$^{fl/fl}$ FGC R26T mice. The image is representative of three independent experiments. **c**, Images of *Aim2*$^{+/+}$ FGC R26T and *Aim2*$^{fl/fl}$ FGC R26T mice and corresponding lymphoid organs of spleen and lymph nodes. **d**, Flow cytometry of $CD4^+FOXP3^+CD25^+$ T_{reg} cells in the thymus, spleen and PLN of *Aim2*$^{+/+}$ FGC R26T and *Aim2*$^{fl/fl}$ FGC R26T mice Representative results (top) and statistical analysis (bottom) of four experiments are shown. **e**, Flow cytometry of $CD4^+$ or $CD8^+$ T cells in the spleen and PLN of *Aim2*$^{+/+}$ FGC R26T and *Aim2*$^{fl/fl}$ FGC R26T mice. Representative results (left) and statistical analysis (right) of four experiments are shown. **f**, **g**, Flow cytometry of naive, effector/memory $CD4^+$ (**f**) and $CD8^+$ (**g**) T cells in the spleen and PLN of *Aim2*$^{+/+}$ FGC R26T and *Aim2*$^{fl/fl}$ FGC R26T mice by assessing CD44 and CD62L expression. Representative results (left for **f**, top for **g**) and statistical analysis (right for **f**, bottom for **g**) of four experiments are shown. **h**, **i**, Flow cytometry of IFNγ-, IL-4- or IL-17A-producing $CD4^+$ cells (**h**) and IFNγ-producing $CD8^+$ T cells (**i**) in *Aim2*$^{+/+}$ FGC R26T and *Aim2*$^{fl/fl}$ FGC R26T mice. Representative results (top) and statistical analysis (bottom) of four experiments are shown. **j**, Statistical summary of IFNγ-, IL-17A-producing $CD4^+Tomato^-$ T_{conv} cells in the PLN (left) and spleen (right) of *Aim2*$^{+/+}$ FGC R26T and *Aim2*$^{fl/fl}$ FGC R26T mice at day 28 of an EAE course. Composite data summarized from three biological replicates. **k**, Statistical summary of IFNγ-, IL-17A-producing $CD4^+Tomato^+$ T_{reg} cells in the PLN (left) and spleen (right) of *Aim2*$^{+/+}$ FGC R26T and *Aim2*$^{fl/fl}$ FGC R26T mice at day 28 of EAE course. Composite data summarized from three biological replicates. **l**, Flow cytometry of Ki67 to analyse proliferation of *Aim2*$^{+/+}$ FGC and *Aim2*$^{fl/fl}$ FGC T_{reg} cells in the PLN, spleen and spinal cord during EAE. Left, representative sample; right, composite data summarized from three biological replicates. **m**, Apoptosis of *Aim2*$^{+/+}$ FGC and *Aim2*$^{fl/fl}$ FGC T_{reg} cells in the spinal cord during EAE was analysed by flow cytometry using annexin V and 7AAD staining. Left, representative sample; right, composite data summarized from three biological replicates. **n**, Flow cytometry of Ki67 to analyse proliferation of *Aim2*$^{+/+}$ FGC and *Aim2*$^{fl/fl}$ FGC T_{reg} cells in the PLN and spleen at steady state. Left, representative sample; right, composite data of five mice of two independent experiments. **o**, Apoptosis of *Aim2*$^{+/+}$ FGC and *Aim2*$^{fl/fl}$ FGC T_{reg} cells in the PLN and spleen at steady state was analysed by flow cytometry using annexin V and 7AAD staining. Left, representative sample; right, composite data of five mice of two independent experiments. Data are mean ± s.e.m. *P* values determined by two-sided *t*-test unless specified.

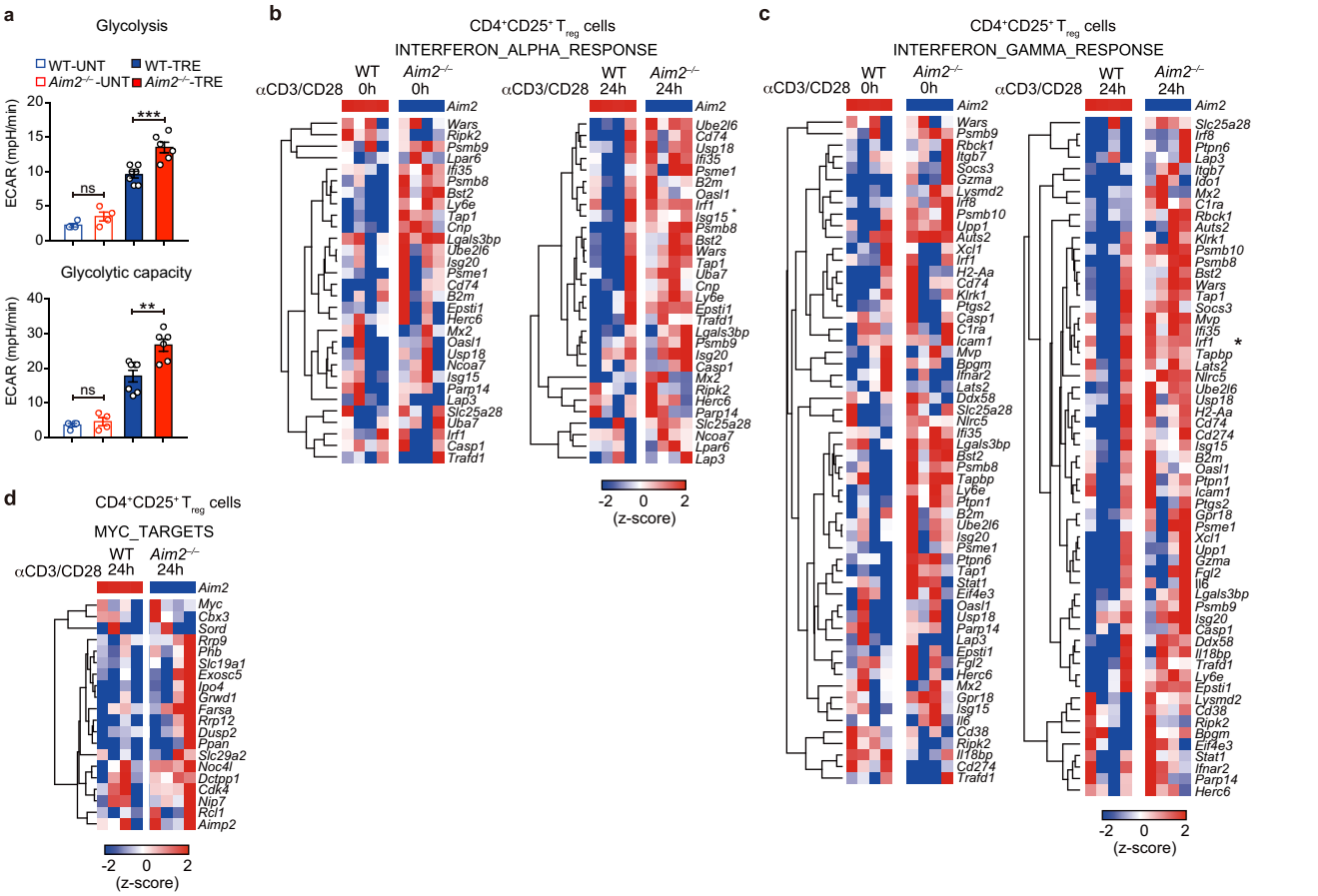

Extended Data Fig. 6 | Enhanced glycolytic, IFN and MYC target signatures are found in *Aim2*$^{-/-}$ T_{reg} cells isolated in vivo. a, Glycolytic activity of wild-type ($n = 7$ biological replicates per group) and *Aim2*$^{-/-}$ ($n = 6$ biological replicates per group) T_{reg} cells untreated (UNT) or treated (TRE) with anti-CD3/CD28 antibodies plus IL-2 (500 U ml^{-1}) for 24 h. Statistics of glycolysis (ECAR rate after glucose addition) and glycolytic capacity (maximal ECAR after subtracting the ECAR rate after exposure to 2-deoxy-D-glucose (2-DG) calculated from Fig. 3a. Data are mean ± s.e.m. $^{**}P < 0.01$, $^{***}P < 0.001$, two-sided *t*-test. **b**, Heat map of IFNα response signature of RNA-seq data from *Aim2*$^{-/-}$ compared to wild-type T_{reg} cells stimulated with anti-CD3/CD28 plus IL-2 (500 U ml^{-1}) at indicated time points (0 or 24 h). **c**, Heat map of IFNγ response signature as described in **b**. **d**, Heat map of MYC target profiles as described in **b**.

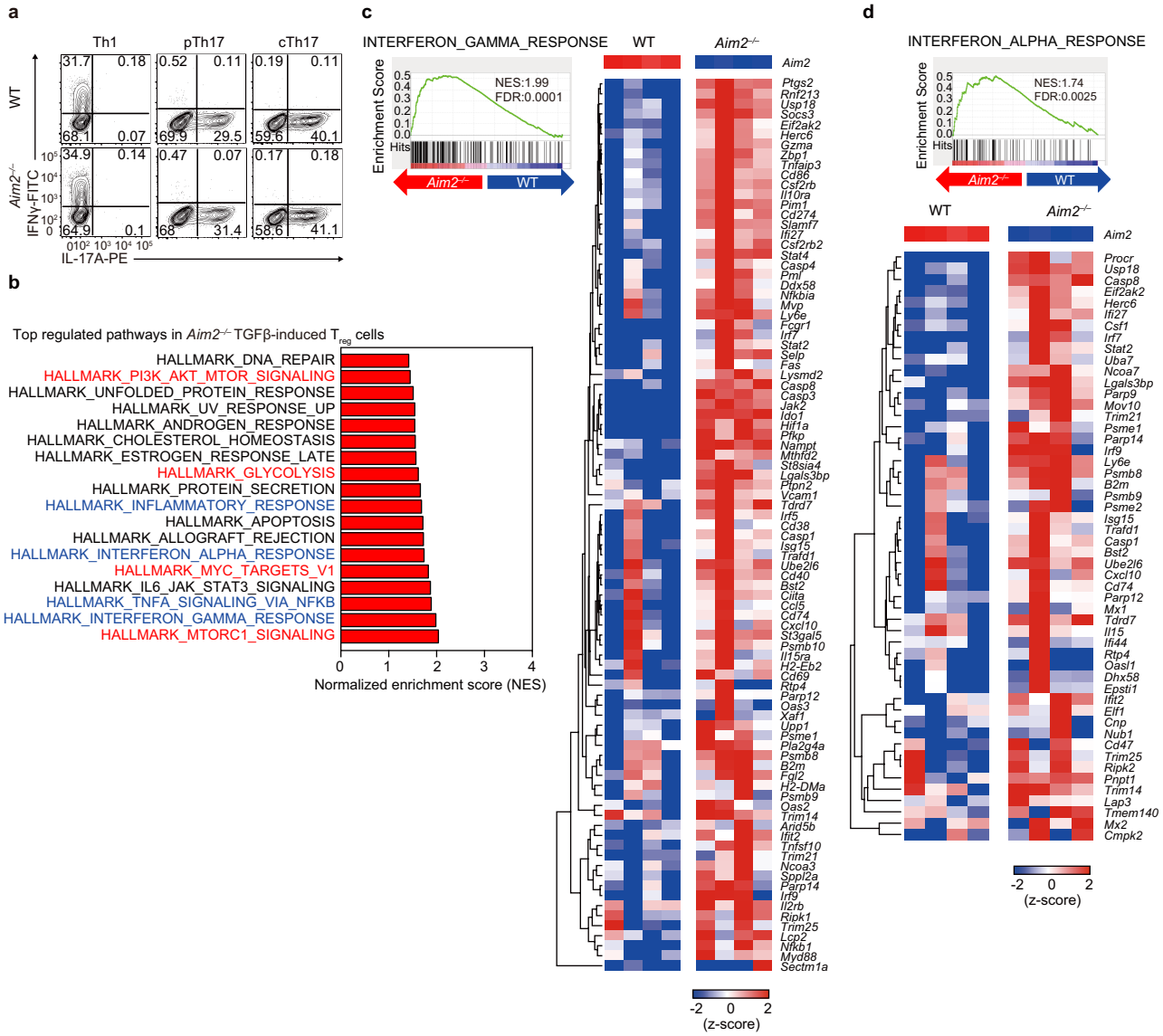

Extended Data Fig. 7 | Enhanced gene signature found in TGFβ-induced *Aim2*$^{-/-}$ T_{reg} cells using RNA-seq analysis. a, Flow cytometry of IFNγ$^+$ or IL-17A$^+$ CD4$^+$ cells from wild-type and *Aim2*$^{-/-}$ mice after four days of differentiation under T_H1, pT_H17 and cT_H17 conditions, respectively, as described in Fig. 4c. Data are representative of four independent experiments. **b**, Summary of top pathways positively enriched in anti-CD3/CD28 activated *Aim2*$^{-/-}$ CD4$^+$ T cells in the presence of TGFβ (2 ng ml^{-1}) and IL-2 (40 U ml^{-1}) for 24 h, by GSEA analysis of the RNA-seq dataset. **c**, **d**, Enrichment of IFNγ (**c**) and IFNα response pathways (**d**) by GSEA (left) and heat map (right) of pathway-related genes in *Aim2*$^{-/-}$ versus wild-type CD4$^+$ T cells stimulated with anti-CD3/CD28 in the presence of TGFβ (2 ng ml^{-1}) and IL-2 (40 U ml^{-1}) for 24 h.

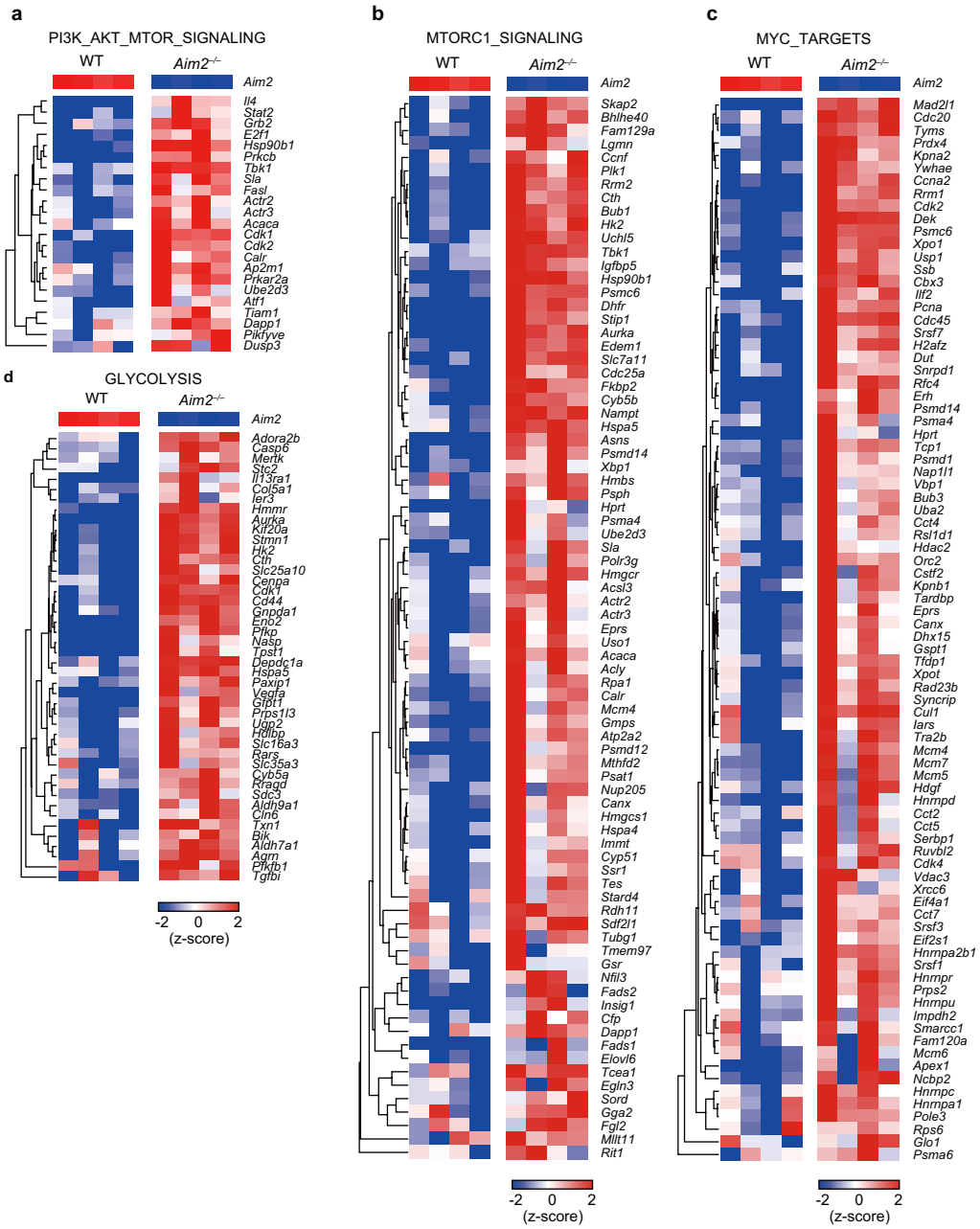

Extended Data Fig. 8 | RNA-seq analysis reveals enhanced mTOR, MYC and glycolytic signatures in TGFβ-induced *Aim2*$^{-/-}$ T_{reg} cells. a, Heat map of PI3K–AKT–mTORC-related gene expression in wild-type and *Aim2*$^{-/-}$ CD4^{+} T cells stimulated with anti-CD3/CD28 in the presence of TGFβ (2 ng ml^{-1}) and IL-2 (40 U ml^{-1}) for 24 h. **b**, Heat map of mTORC1 signalling-related gene expression, with samples described in **a**. **c**, Heat map of MYC target-related gene expression, with samples described in **a**. **d**, Heat map of glycolysis-related gene expression, with samples described in **a**.

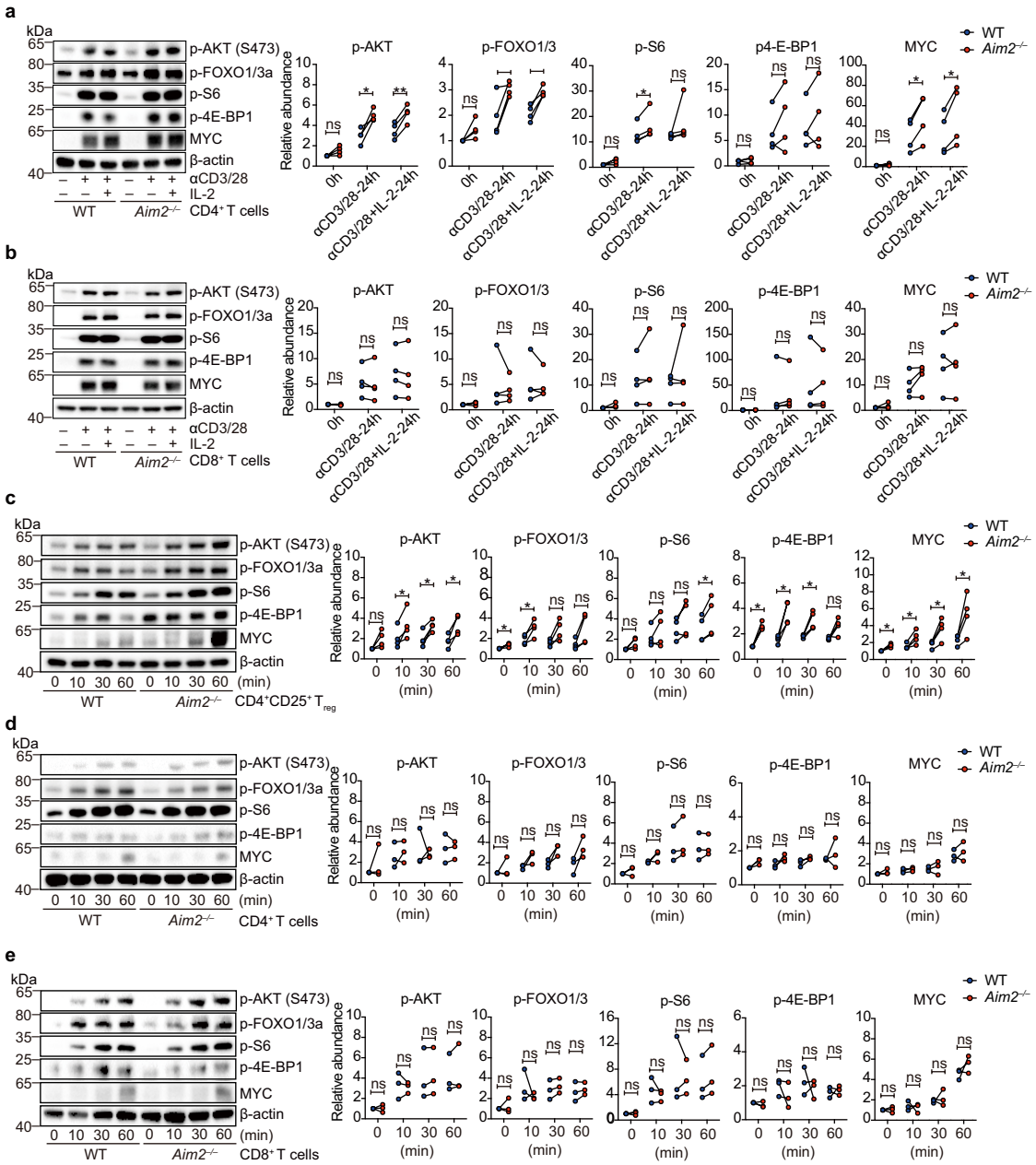

Extended Data Fig. 9 | AKT–mTOR signalling in wild-type and *Aim2*$^{-/-}$ T_{reg}, CD4$^+$ and CD8$^+$ T cells. a, **b**, Immunoblot analysis of p-AKT(S473), p-FOXO1, p-FOXO3A, p-S6, p-4E-BP1, MYC and β-actin in wild-type and *Aim2*$^{-/-}$ CD4$^+$ T cells (**a**) or CD8$^+$ T cells (**b**) stimulated with anti-CD3/CD28 plus IL-2 (40 U ml^{-1}) for 24 h. **c**–**e**, Immunoblot analysis of p-AKT(S473), p-FOXO1, p-FOXO3A, p-S6, p-4E-BP1, MYC and β-actin in wild-type and *Aim2*$^{-/-}$ T_{reg} cells (**c**) stimulated with anti-CD3/CD28 plus IL-2 (500 U ml^{-1}), or CD4$^+$ (**d**) and CD8$^+$ (**e**) T cells stimulated with anti-CD3/CD28 plus IL-2 (40 U ml^{-1}) for indicated time points. Left, representative results; right, quantification for statistics by densitometric analysis using Image Lab software; $n = 4$ experiments (**a**–**c**); $n = 3$ experiments (**d**, **e**). $^*P < 0.05$, $^{**}P < 0.01$, analysed by two-sided paired *t*-test.

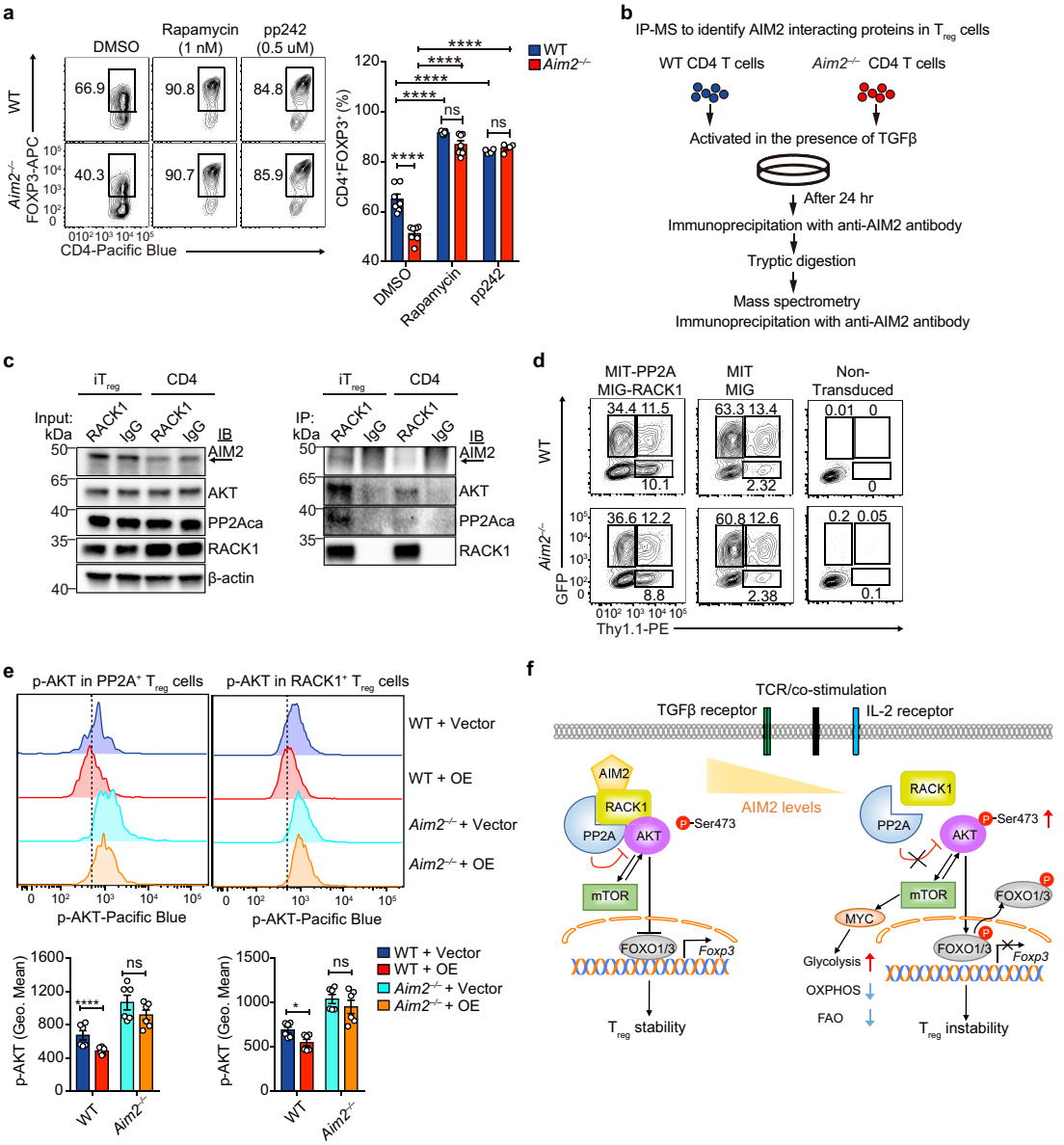

Extended Data Fig. 10 | AIM2 interacts with the RACK1–PP2A–AKT complex and is critical to regulate AKT–mTOR signalling for T_{reg} cell generation. **a**, Flow cytometry analysis of FOXP3 in wild-type and *Aim2*$^{-/-}$ CD4$^+$ T cells stimulated by anti-CD3/CD28 plus IL-2 (40 U ml^{-1}) and TGFβ (2 ng ml^{-1}) and then cultured with DMSO ($n = 4$ biological replicates/group), rapamycin (1 nM) ($n = 7$ biological replicates/group), or pp242 (0.5 μM) ($n = 7$ biological replicates/group) for 96 h. Results are representative of three independent experiments. *P* value by one-way ANOVA with Tukey's multiple comparisons test. **b**, Schema of IP–MS approach to identify AIM2-interacting proteins in TGFβ-induced T_{reg} cells. Wild-type and *Aim2*$^{-/-}$ naive CD4$^+$ T cells were activated with anti-CD3/CD28 in the presence of TGFβ (2 ng ml^{-1}) and IL-2 (40 U ml^{-1}) for 24 h and protein lysates from each group were collected for further IP–MS analysis. **c**, Interaction of AIM2 and RACK1 detected by immunoprecipitation using anti-RACK1 antibody or anti-IgG as control in TGFβ-induced T_{reg} (iT_{reg}) cells and CD4$^+$ T cells, and immunoblotted with different antibodies, including anti-PP2Aca, anti-AKT, anti-RACK1 and anti-AIM2. Arrow points to the AIM2 protein. Results are representative of three independent experiments. **d**, Wild-type and *Aim2*$^{-/-}$ CD4$^+$ T cells were stimulated with anti-CD3 and CD28 plus IL-2 (40 U ml^{-1}) and TGFβ (2 ng ml^{-1}) for 24 h and transduced either with MIT-PP2A and MIG-RACK1, or with MIT and MIG vector controls. The cells were collected 3 days after virus transduction. The populations expressing PP2A (Thy1.1$^+$), RACK1 (GFP$^+$) and both (Thy1.1$^+$GFP$^+$) were identified by flow cytometry. **e**, Flow cytometry of p-AKT of wild-type and *Aim2*$^{-/-}$ T_{reg} cells that overexpressed PP2A (Thy1.1$^+$) or RACK1 (GFP$^+$) compared to corresponding vector controls. Representative FACS plots (top) and statistical analysis (bottom) of six experiments are shown. *P* value by multiple unpaired *t*-test with Holm–Sidak method. **f**, Model for AIM2 function shows that AIM2 facilitates the interaction between RACK1 and PP2A phosphatase, causing dephosphorylation of AKT to restrain the activity of the mTOR pathway, therein promoting *Foxp3* expression and T_{reg} cell stability. Data are mean ± s.e.m. *$P < 0.05$, ****$P < 0.0001$.